

# Global simulations of kinetic-magnetohydrodynamic processes with energetic electrons in tokamak plasmas

J. Bao<sup>1,2,\*</sup>, W.L. Zhang<sup>1,2,3,\*</sup> , D. Li<sup>1,2,3</sup>, Z. Lin<sup>4</sup>, Z.Y. Qiu<sup>5</sup> , W. Chen<sup>6</sup> , X. Zhu<sup>7</sup> , J.Y. Cheng<sup>8</sup>, C. Dong<sup>1,2</sup> and J.T. Cao<sup>1,2</sup>

<sup>1</sup> Beijing National Laboratory for Condensed Matter Physics and CAS Key Laboratory of Soft Matter Physics, Institute of Physics, Chinese Academy of Sciences, Beijing 100190, China

<sup>2</sup> University of Chinese Academy of Sciences, Beijing 100049, China

<sup>3</sup> Songshan Lake Materials Laboratory, Dongguan, Guangdong 523808, China

<sup>4</sup> University of California, Irvine, CA 92697, United States of America

<sup>5</sup> Institute for Fusion Theory and Simulation and Department of Physics, Zhejiang University, Hangzhou 310027, China

<sup>6</sup> Southwestern Institute of Physics, PO Box 432, Chengdu 610041, China

<sup>7</sup> Advanced Energy Research Center, Shenzhen University, Shenzhen 518060, China

<sup>8</sup> Department of Physics, University of Colorado at Boulder, Boulder, CO 80309, United States of America

E-mail: [jbao@iphy.ac.cn](mailto:jbao@iphy.ac.cn) and [wzhang@iphy.ac.cn](mailto:wzhang@iphy.ac.cn)

Received 1 April 2023, revised 9 October 2023

Accepted for publication 20 October 2023

Published 15 November 2023



## Abstract

The energetic electrons (EEs) produced from auxiliary heatings have been found to destabilize various Alfvén eigenmodes (AEs) in recent experiments. To investigate EE relevant kinetic-magnetohydrodynamic (MHD) processes, a global fluid-kinetic hybrid model is formulated and verified in this work, which consists of Landau-fluid bulk plasmas and drift-kinetic EEs that incorporates the dominant damping and drive mechanisms, respectively. The numerical capability of Landau-fluid bulk plasmas is obtained based on a well-benchmarked eigenvalue code multiscale analysis for plasma stability (MAS) using general geometry (Bao *et al* 2023 *Nucl. Fusion* **63** 076021), and the comprehensive EE responses to the low frequency ( $\omega \ll \Omega_{ci}$ ) MHD fluctuations are analytically derived and implemented in MAS, which not only cover contributions from trapped and passing particles, but also take into account the effects of adiabatic fluid convection and non-adiabatic kinetic compression. The linear properties of EE-driven beta-induced AEs (e-BAEs) are systematically studied using both MAS model and gyrokinetic toroidal code (GTC) particle-in-cell simulations. Building on the good agreements on the mode structure and dispersion relation, several key issues of e-BAE physics are analyzed and discussed, including the parametric dependences of e-BAE stability on EE mass, temperature

\* Authors to whom any correspondence should be addressed.



Original Content from this work may be used under the terms of the [Creative Commons Attribution 4.0 licence](https://creativecommons.org/licenses/by/4.0/). Any further distribution of this work must maintain attribution to the author(s) and the title of the work, journal citation and DOI.

and density with corresponding phase space dynamics, EE non-perturbative effects on the symmetry breaking of mode structure, and the EE density and temperature thresholds for e-BAE excitation that overcome bulk plasma damping. With these efforts, the upgraded MAS model is superior than initial-value simulations restricted by stringent electron Courant condition for fast linear analyses of most EE-AE problems with  $\omega \ll \Omega_{ci}$ , of which wave-particle resonance can be used to analyze the analogous effect of alpha particle driven AEs in future fusion reactor.

Keywords: kinetic-magnetohydrodynamic, energetic electrons, Alfvén eigenmodes, non-perturbative, global eigenvalue approach

(Some figures may appear in colour only in the online journal)

## 1. Introduction

Various Alfvén eigenmodes (AEs) can be destabilized by energetic particles (EPs) through abundant channels of wave-particle resonances in tokamak plasmas, and the relevant kinetic-magnetohydrodynamic (MHD) processes are of great interest from aspects of experiment, theory and simulation [1, 2]. In particular, the AEs driven by energetic ions (EIs) are widely observed in experiments, and most linear and nonlinear properties have been studied and understood over the past four decades [3, 4], while the AEs driven by energetic electrons (EEs) are much less explored until recently, i.e. not only the single mode dynamics of EE-driven beta-induced AE (e-BAE) [5, 6] and EE-driven toroidal AE (e-TAE) [7–11] are confirmed in HL-2A and EAST tokamaks, but also the experimental evidences of the nonlinear mode-mode interaction between e-TAE and geodesic acoustic mode have been demonstrated [12]. Understanding the excitation mechanism of these EE-driven AEs and required plasma condition are important for clarifying the underlying physics of relevant experimental phenomena, meanwhile, the resonance interactions between EEs and MHD modes in present-day tokamaks can be used to extrapolate alpha particle physics in future fusion reactor characterized by similarly small dimensionless orbits (i.e. the particle orbit width normalized by minor radius), and EEs can also be produced in future burning plasmas through collisional heating by alpha particles, acceleration by DC electric field along parallel direction, and collisionless heating by radio frequency waves such as electron cyclotron resonance heating (ECRH) and lower hybrid current drive (LHCD).

Both theoretical and numerical efforts have been made to explain the EE-driven AEs in experiments. It has been shown that the bounce-averaged dynamics of EEs are responsible for the resonant interaction with MHD modes characterized by much lower frequency than EE bounce and transit frequencies ( $\omega \ll \omega_{b,h} < \omega_{t,h}$ ) from the perspective of first-principle gyrokinetic framework [13]. Recently, the bounce-kinetic EE model is also applied to the theoretical studies of linear excitation of e-BAE [14, 15] and the nonlinear excitation of zonal flow by pump e-BAE [16], which successfully reveal that the dominant destabilizing mechanism of e-BAE is attributed to the EE precessional drift resonance, as well as the important role of resonant EEs on the nonlinear mode-mode coupling. At the same time, both the gyrokinetic particle-in-cell

(PIC) simulation [17, 18] and kinetic-MHD hybrid simulation [19, 20] have been performed to study the e-BAE and e-TAE with drift-kinetic description of EE dynamics, and the deeply-trapped EE response is found to have a maximal resonance island with e-BAE [17] and e-TAE [19] propagating along the electron diamagnetic direction, while the passing EEs are responsible for the high frequency EAE [19]. However, regarding to the shot-to-shot analysis in experiments, the ballooning theory relies on the scale separation and is difficult to incorporate the complex geometry, and the initial value simulation using drift-kinetic EEs suffers the stringent and unnecessary numerical constraints due to the electron Courant condition with realistic electron-ion mass ratio [21]. For comparison, the eigenvalue approach using magnetic coordinates is more efficient for the plasma stability analysis with realistic geometry, such as LIGKA [22], NOVA-K [23] and CASTOR-K [24], which mostly focus on EI physics rather than EE physics. Motivated by previous theories and simulations that have provided the fundamental physics insights on the linear excitation of AEs by EE precessional drift resonance, we construct kinetic-MHD model focusing on EE physics based on eigenvalue approach in this work, which combines the necessary EE drive, bulk plasma damping and realistic geometry together for analyzing and optimizing experiments by fast parameter scans.

Recently, the eigenvalue code multiscale analysis for plasma stability (MAS) has been developed for plasma stability analysis in experimental geometry based on a five-field Landau-fluid model description of bulk plasma [25], which captures the essential kinetic effects of ion finite Larmor radius (FLR), ion and electron diamagnetic drifts and Landau dampings on the same footing with MHD-fluid responses. Meanwhile, comprehensive benchmarks have been carried out for the code verification and validation that covers ion-scale drift wave instabilities (i.e. ion temperature gradient mode and kinetic ballooning mode), ideal internal kink mode and various AEs, and MAS results show reasonable agreements with other gyrokinetic and kinetic-MHD hybrid codes [25, 26]. This work extends MAS Landau-fluid formulation with EE physics described by drift-kinetic equation, and incorporates both bulk plasma damping and EE drive effects in a non-perturbative manner that are necessary for determining EE density and temperature thresholds for AE excitation. Meanwhile, an improved deeply-trapped approximation is proposed to evaluate the dominant precessional drift resonance of EE species, which greatly speeds up the calculations

with acceptable accuracy for the bounce-averaged dynamics of most trapped EEs. Applying the upgraded MAS model, the e-BAE is investigated as an example of EE-driven AEs in the model validity regime of  $\omega \ll \Omega_{ci}$ . Moreover, we show the similarities of EEs in present-day tokamaks and alpha particles in burning plasmas on their small dimensionless orbits and resonances with AEs based on experimental parameters. The remainder of this paper is organized as follows. The formulation of upgraded MAS model is introduced in section 2. In section 3, we show the theoretical ordering estimations of the newly added EE-related terms in both electromagnetic and electrostatic limits. In section 4, we present the numerical comparisons of e-BAE mode structure and dispersion relation between MAS model and gyrokinetic toroidal code (GTC) PIC simulations. The effects of EE mass, density and temperature on e-BAE stability are analyzed with corresponding phase space dynamics. The summary is given in section 5. Moreover, the typical EP orbits and resonances with AEs in present-day tokamaks and future fusion reactor are shown in appendix A. The characteristics of EI-driven BAE (i-BAE) are revisited and compared with e-BAE in appendix B.

## 2. Physics model

### 2.1. Drift-kinetic equation for EE

Considering the smallness of realistic electron mass, we apply the drift-kinetic model for EE species that induces the necessary Landau resonance while ignores the FLR effect. The linearized drift-kinetic equation in five dimensional phase space uses guiding center position  $\mathbf{R}$ , magnetic moment  $\mu = m_e v_{\perp}^2 / 2B_0$  and parallel velocity  $v_{\parallel}$  as independent variables, which reads

$$L_0 \delta f_h + \delta L^L f_{h0} = 0, \quad (1)$$

where  $\delta f_h$  and  $f_{h0}$  are the EE perturbed and equilibrium distributions,  $L_0$  and  $\delta L^L$  are the equilibrium and linear perturbed propagators given by

$$L_0 = \frac{\partial}{\partial t} + (v_{\parallel} \mathbf{b}_0 + \mathbf{v}_d) \cdot \nabla - \frac{\mu}{m_e B_0} \mathbf{B}_0^* \cdot \nabla B_0 \frac{\partial}{\partial v_{\parallel}}$$

and

$$\delta L^L = \left( v_{\parallel} \frac{\delta \mathbf{B}}{B_0} + \mathbf{v}_E \right) \cdot \nabla - \left[ \frac{\mu}{m_e B_0} \delta \mathbf{B} \cdot \nabla B_0 + \frac{q_e}{m_e} \left( \frac{\mathbf{B}_0^*}{B_0} \cdot \nabla \delta \phi + \frac{1}{c} \frac{\partial \delta A_{\parallel}}{\partial t} \right) \right] \frac{\partial}{\partial v_{\parallel}},$$

$q_e$  and  $m_e$  are electron charge and mass,  $\delta \phi$  and  $\delta A_{\parallel}$  are the electrostatic potential and parallel vector potential,  $\mathbf{b}_0 = \mathbf{B}_0 / B_0$  is the unit vector of the equilibrium magnetic field,  $\mathbf{B}_0^* = \mathbf{B}_0 + (B_0 v_{\parallel} / \Omega_{ce}) \nabla \times \mathbf{b}_0$ ,  $\Omega_{ce} = q_e B_0 / c m_e$  is the electron cyclotron frequency,  $\delta \mathbf{B} = \nabla \times (\delta A_{\parallel} \mathbf{b}_0)$  represents the perturbed magnetic field, and  $\mathbf{v}_d$  and  $\mathbf{v}_E$  are the magnetic drift and  $\mathbf{E} \times \mathbf{B}$  drift, which read

$$\mathbf{v}_d = \frac{v_{\parallel}^2}{\Omega_{ce}} \nabla \times \mathbf{b}_0 + \frac{\mu \mathbf{b}_0 \times \nabla B_0}{m_e \Omega_{ce}}$$

and

$$\mathbf{v}_E = \frac{c \mathbf{b}_0 \times \nabla \delta \phi}{B_0}.$$

For EE-driven Alfvénic instabilities, the linear unstable spectra can be influenced by the EE velocity distribution relying on the specific auxiliary heating methods such as ECRH and LHCD [13]. Though the EE velocity distribution is not unique in experiments, we define effective EE temperatures for analysis convenience, namely,  $T_{\parallel h0} = \int m_e v_{\parallel}^2 f_{h0} d\mathbf{v} / n_{h0}$  and  $T_{\perp h0} = \int \mu B_0 f_{h0} d\mathbf{v} / n_{h0}$ , where  $n_{h0} = \int f_{h0} d\mathbf{v}$  is the EE density. In current work that illustrates the model scheme, we utilize the isotropic Maxwellian to approximate the EE equilibrium distribution, i.e.  $f_{h0} = n_{h0} \left( \frac{m_e}{2\pi T_{h0}} \right)^{3/2} \exp\left(-\frac{m_e v_{\parallel}^2 + 2\mu B_0}{2T_{h0}}\right)$  with  $T_{h0} = T_{\parallel h0} = T_{\perp h0}$ , and other EE velocity distributions such as slowing-down will be investigated in future work. We further separate the perturbed distribution  $\delta f_h$  in equation (1) into the adiabatic part and non-adiabatic part

$$\delta f_h = \delta f^A + \delta K. \quad (2)$$

The adiabatic distribution is determined by the terms related to fast parallel dynamics in equation (1), which are in the leading order of  $\omega / (k_{\parallel} v_{\parallel})$  as

$$v_{\parallel} \mathbf{b}_0 \cdot \nabla \delta f^A + v_{\parallel} \frac{1}{B_0} \delta \mathbf{B} \cdot \nabla f_{h0} \Big|_{v_{\perp}} - \frac{q_e}{m_e} \left( \mathbf{b}_0 \cdot \nabla \delta \phi + \frac{1}{c} \frac{\partial \delta A_{\parallel}}{\partial t} \right) \frac{\partial f_{h0}}{\partial v_{\parallel}} = 0, \quad (3)$$

where  $\nabla f_{h0} \Big|_{v_{\perp}} = (\nabla n_{h0} / n_{h0}) f_{h0} + [(m_e v_{\parallel}^2 + 2\mu B_0) / (2T_{h0}) - 3/2] (\nabla T_{h0} / T_{h0}) f_{h0}$  and  $\partial f_{h0} / \partial v_{\parallel} = -(m_e v_{\parallel} / T_{h0}) f_{h0}$  for Maxwellian  $f_{h0}$ . We define a new variable  $\delta \psi$  according to

$$\frac{\partial \delta A_{\parallel}}{\partial t} = -c \mathbf{b}_0 \cdot \nabla \delta \psi, \quad (4)$$

and  $\delta \psi = \omega \delta A_{\parallel} / (c k_{\parallel})$  is adopted for following derivations with convenience. Substituting equation (4) into equation (3) and using the ansatz  $\partial_t = -i\omega$  and  $\mathbf{b}_0 \cdot \nabla = i k_{\parallel}$ ,  $\delta f^A$  can be readily solved from equation (3)

$$\delta f^A = -\frac{q_e}{T_{h0}} (\delta \phi - \delta \psi) f_{h0} - \frac{q_e}{T_{h0}} \delta \psi \left[ \frac{\omega_{*n,h}}{\omega} + \left( \frac{m_e v_{\parallel}^2 + 2\mu B_0}{2T_{h0}} - \frac{3}{2} \right) \frac{\omega_{*T,h}}{\omega} \right] f_{h0}, \quad (5)$$

where  $\omega_{*n,h} = -i \frac{c T_{h0}}{q_e B_0} \mathbf{b}_0 \times \frac{\nabla n_{h0}}{n_{h0}} \cdot \nabla$  and  $\omega_{*T,h} = -i \frac{c}{q_e B_0} \mathbf{b}_0 \times \nabla T_{h0} \cdot \nabla$ . Note that the form of  $\delta f^A$  in equation (5) is also adopted in gyrokinetic theory [27, 28] and simulation [29], which contains both the adiabatic response to the parallel electric field and convective response to the perturbed magnetic field.

From equations (1), (2) and (5), the governing equation for the non-adiabatic distribution  $\delta K$  can be written as

$$\left[ -i(\omega - \omega_d) + v_{||} \mathbf{b}_0 \cdot \nabla - \frac{\mu}{m_e B_0} \mathbf{B}_0^* \cdot \nabla B_0 \frac{\partial}{\partial v_{||}} \right] \delta K = -i \frac{q_e}{T_{h0}} \omega \left( 1 - \frac{\omega_{*p,h}}{\omega} \right) (\delta\phi - \delta\psi) f_{h0} - i \frac{q_e}{T_{h0}} \omega_d \left( 1 - \frac{\omega_{*p,h}}{\omega} \right) \delta\psi f_{h0} \quad (6)$$

where  $\omega_d = -i\mathbf{v}_d \cdot \nabla$  is the magnetic drift frequency and  $\omega_{*p,h} = \omega_{*n,h} + [(m_e v_{||}^2 + 2\mu B_0)/(2T_{h0}) - 3/2]\omega_{*T,h}$  is the diamagnetic frequency. It is also noted that  $C_s/V_A = \sqrt{\beta_e/2}$ ,  $v_{\text{the}}/V_A = \sqrt{\beta_e m_i/(2m_e)}$  and  $C_s/v_{\text{the}} = \sqrt{m_e/m_i}$ , where  $C_s$ ,  $V_A$  and  $v_{\text{the}}$  denote ion sound speed, Alfvén speed and electron thermal speed, respectively,  $\beta_e = 8\pi n_e T_e/B_0^2$  and  $m_e/m_i \ll \beta_e \ll 1$  in tokamak plasmas. With these orderings, one can solve  $\delta K$  from equation (6) for passing and trapped EE particles, respectively.

First, in the regime of  $k_{||} v_{||} \gg \omega \sim \omega_d$  for passing EE particles, equation (6) reduces to

$$v_{||} \mathbf{b}_0 \cdot \nabla \delta K^p = -i \frac{q_e}{T_{h0}} \omega \left( 1 - \frac{\omega_{*p,h}}{\omega} \right) (\delta\phi - \delta\psi) f_{h0} - i \frac{q_e}{T_{h0}} \omega_d \left( 1 - \frac{\omega_{*p,h}}{\omega} \right) \delta\psi f_{h0} \quad (7)$$

where we have  $\delta K^p \sim 0$  since  $v_{||} \mathbf{b}_0 \cdot \nabla \rightarrow \infty$ , and  $\delta K^p$  contribution to perturbed density and pressure can be ignored. However,  $v_{||} \delta K^p$  is finite and gives rise to a fraction of parallel current density carried by passing EEs.

Second, EE particles interact and exchange energy with MHD modes primarily through the precessional drift resonance, while the bounce and transit frequencies are too high to resonate with typical AEs, as demonstrated and confirmed by recent theories and simulations [14, 16, 17, 19]. According to these characteristics, we have  $\omega \sim \bar{\omega}_d \ll \omega_b$  for trapped EE particles, where  $\omega_b = 2\pi/\tau_b$  and  $\tau_b = \oint (dl/v_{||})$  is the bounce period, and  $\bar{\omega}_d = \oint \omega_d (dl/v_{||})/\tau_b$  is the precession frequency, and  $l$  is the traveled distance of trapped particle along magnetic field line in one bounce motion period. Defining  $\omega_b \partial/\partial \eta = v_{||} \mathbf{b}_0 \cdot \nabla$  for trapped particle with  $\eta$  being the bounce angle coordinate and  $d\eta = \omega_b (dl/v_{||})$ , we can transform equation (6) into banana orbit center frame using  $\delta K^t = \delta K_b^t \exp(i\alpha)$  with  $\alpha = -\int d\eta (\omega_d - \bar{\omega}_d)/\omega_b$  [30], and then perform bounce average  $\overline{(\dots)} = \oint (\dots) (dl/v_{||})/\tau_b$ , i.e.  $\overline{(\dots)} = \oint (\dots) d\eta/2\pi$ . Note that  $\omega_d - \bar{\omega}_d \ll \omega_b$ , we have  $\exp(i\alpha) \approx 1$  which means that  $\delta K^t \simeq \delta K_b^t$  and finite orbit width (FOW) can be dropped for EE particles as a higher order effect, then the solution of trapped EE non-adiabatic response is

$$\delta K^t \simeq \delta K_b^t = \underbrace{\frac{\omega}{\omega - \bar{\omega}_d} \frac{q_e}{T_{h0}} \left( 1 - \frac{\omega_{*p,h}}{\omega} \right) (\bar{\delta\phi} - \bar{\delta\psi}) f_{h0}}_{\{I\}} + \underbrace{\frac{1}{\omega - \bar{\omega}_d} \frac{q_e}{T_{h0}} \left( 1 - \frac{\omega_{*p,h}}{\omega} \right) \bar{\omega}_d \bar{\delta\psi} f_{h0}}_{\{II\}} \quad (8)$$

where term {I} corresponds to the non-ideal MHD effect  $\Delta\phi = \delta\phi - \delta\psi$ , and term {II} drives the bad-curvature instabilities with a minimum threshold  $\omega_{*p,h} > \omega$ . For most instabilities in tokamak characterized with ‘flute-like’ mode structures,  $\delta\phi$  and  $\delta\psi$  peak around the rational surfaces where  $|nq - m| \ll 1$ , then we can further simplify equation (8) using  $\bar{\delta\phi} \approx \delta\phi$ ,  $\bar{\delta\psi} \approx \delta\psi$ , and  $\bar{\omega}_d \bar{\delta\psi} \approx \bar{\omega}_d \delta\psi$ . The more general validity regime of these simplifications is  $\exp[-i(m - nq)\theta] \approx 1$  [16], which only requires  $|\theta| \ll 1/|nq - m|$ . Thus, for instabilities with moderate  $|nq - m| \leq 1$  that deviate from rational surface, one can reduce trapped EE fraction by decreasing the  $\theta$  domain of banana orbit mirror throat to more deeply-trapped regime, which still hold  $\bar{\delta\phi} \approx \delta\phi$ ,  $\bar{\delta\psi} \approx \delta\psi$ , and  $\bar{\omega}_d \bar{\delta\psi} \approx \bar{\omega}_d \delta\psi$  for model accuracy. (Note that these simplifications are applied for deriving the EE moments in section 2.2).

## 2.2. The EE moments

To couple drift-kinetic EEs with the existing Landau-fluid model of bulk plasmas, one needs to derive the EE continuity equation by integrating equation (1) in velocity space using  $\langle \dots \rangle_v = \int d\mathbf{v} = \frac{2\pi B_0}{m_e} \int dv_{||} d\mu$ , i.e.

$$\frac{\partial \delta n_h}{\partial t} + \mathbf{v}_E \cdot \nabla n_{h0} + n_{h0} \mathbf{B}_0 \cdot \nabla \left( \frac{\delta u_{||h}}{B_0} \right) + 2cn_{h0} \nabla \delta\phi \cdot \frac{\mathbf{b}_0 \times \boldsymbol{\kappa}}{B_0} + \frac{c}{q_e} \nabla \cdot (\delta P_{||h}^A + \delta P_{\perp h}^A) \cdot \frac{\mathbf{b}_0 \times \boldsymbol{\kappa}}{B_0} + \langle \mathbf{v}_d \cdot \nabla \delta K \rangle_v = 0, \quad (9)$$

where

$$\delta n_h = \int (\delta f^A + \delta K) d\mathbf{v}, \quad (10)$$

$$n_{h0} \delta u_{||h} = \int v_{||} (\delta f^A + \delta K) d\mathbf{v}, \quad (11)$$

$$\delta P_{||h}^A = \int m_e v_{||}^2 \delta f^A d\mathbf{v} = -q_e n_{h0} (\delta\phi - \delta\psi) - q_e n_{h0} \left( \frac{\omega_{*n,h}}{\omega} + \frac{\omega_{*T,h}}{\omega} \right) \delta\psi \quad (12)$$

and

$$\delta P_{\perp h}^A = \int \mu B_0 \delta f^A d\mathbf{v} = -q_e n_{h0} (\delta\phi - \delta\psi) - q_e n_{h0} \left( \frac{\omega_{*n,h}}{\omega} + \frac{\omega_{*T,h}}{\omega} \right) \delta\psi \quad (13)$$

Taking the moment of equation (5), the adiabatic components in equations (10) and (11) are obtained as

$$\delta n_h^A = \int \delta f^A d\mathbf{v} = -\frac{q_e n_{h0}}{T_{h0}} (\delta\phi - \delta\psi) - \frac{q_e n_{h0}}{T_{h0}} \frac{\omega_{*n,h}}{\omega} \delta\psi \quad (14)$$

and

$$\delta u_{||h}^A = \frac{1}{n_{h0}} \int v_{||} \delta f^A d\mathbf{v} = 0, \quad (15)$$

Equations (12)–(15) are referred to as adiabatic EE moments, where the superscript ‘A’ stands for adiabatic.

Then we shall derive the non-adiabatic EE moments. Since the passing EEs move much faster than Alfvén speed of which response is almost adiabatic to shear Alfvén wave and ion sound wave,  $\delta K^p$  in equation (7) does not contribute to density and pressure perturbations but can lead to a finite current in high- $v_{||}$  regime. However, the precessional drift of trapped EE can be close to or below the Alfvén speed, and  $\delta K^t$  in equation (8) are responsible for the non-adiabatic EE density and pressure. Moreover, it has been shown that the deeply-trapped EEs can effectively interact with most drift-type instabilities through precessional drift resonance [14, 17, 19], thus we apply the deeply-trapped approximation for computing the precession frequency in equation (8)

$$\bar{\omega}_d \approx \omega_{d0}, \quad (16)$$

where  $\omega_{d0} = \omega_d|_{\theta=0}$  is the magnetic drift frequency at the outer midplane which only contains the normal curvature related term, while the geodesic curvature related term vanishes in the bounce-averaged dynamics and does not contribute to the precessional drift resonance [31]. The form of  $\omega_{d0}$  in general flux coordinates is given by equation (69), and the validation of deeply-trapped approximation on precession frequency is also shown in section 4. Based on the deeply-trapped approximation, the last term in equation (9) can be written as

$$\langle \mathbf{v}_d \cdot \nabla \delta K \rangle_v \simeq \langle \mathbf{v}_d \cdot \nabla \delta K^t \rangle_v = i \frac{2}{T_{h0}} \omega_{D0,h} \delta P_h^{NA} \quad (17)$$

where  $\omega_{D0,h} = -i \frac{c T_{h0}}{q_e B_0} \mathbf{b}_0 \times \boldsymbol{\kappa} \cdot \nabla|_{\theta=0}$ , and  $\delta P_h^{NA} \simeq \frac{1}{2} \int_{\text{trap}} \delta K^t E d\mathbf{v}$  represents the non-adiabatic EE pressure. We use pitch angle  $\lambda = \mu B_a / (m_e E)$  and energy per unit mass  $E = v^2/2$  as the two dimensions  $(\lambda, E)$  of velocity space instead of  $(v_{||}, \mu)$ , where  $B_a$  is the on-axis magnetic field strength, then the velocity space integration with trapped particles becomes

$$\int_{\text{trap}} d\mathbf{v} = \sqrt{2\pi} \frac{B_0}{B_a} \sum_{\sigma} \int_{\lambda_{\text{low}}}^{B_a/B_0} \frac{1}{\sqrt{\left(1 - \lambda \frac{B_0}{B_a}\right)}} d\lambda \int_0^{+\infty} \sqrt{E} dE, \quad (18)$$

where  $\sigma = \text{sign}(v_{||})$ , and  $B_a/B_{\text{max}} \leq \lambda_{\text{low}} \leq B_a/B_0$  is the lower cutoff of trapped particle pitch angle. For Maxwellian equilibrium distribution  $f_{h0} = n_{h0} \left(\frac{m_e}{2\pi T_{h0}}\right)^{3/2} \exp\left(-\frac{m_e E}{T_{h0}}\right)$ , the trapped particle fraction  $f_t$  at  $B_0$  location can be expressed as

$$f_t = \frac{1}{n_{h0}} \int_{\text{trap}} f_{h0} d\mathbf{v} = \sqrt{1 - \lambda_{\text{low}} \frac{B_0}{B_a}}. \quad (19)$$

By counting all trapped particles at  $B_0$  location with  $\lambda_{\text{low}} = B_a/B_{\text{max}}$ , it is seen that  $f_t = 0$  in the high field side with  $B_0 = B_{\text{max}}$  and  $f_t = \sqrt{1 - B_{\text{min}}/B_{\text{max}}}$  in the low field side with  $B_0 = B_{\text{min}}$ . Compared to former gyrokinetic theory that applies  $f_t \approx \sqrt{2\epsilon}$  (where  $\epsilon = r/R_0$ ) and ignores poloidal variation [31], equation (19) has both radial and poloidal dependences and reflects the realistic trapped particle distribution in the poloidal

plane. In general, equation (18) can be simplified when the integrands do not rely on  $\lambda$

$$\int_{\text{trap}} d\mathbf{v} = 4\sqrt{2\pi} f_t \int_0^{+\infty} \sqrt{E} dE. \quad (20)$$

Thus, with the assumption in equation (16), it is straightforward to integrate  $\delta K^t$  in equation (8) in velocity space using equation (20), and the non-adiabatic density and pressure perturbations are derived explicitly

$$\begin{aligned} \delta n_h^{NA} &= \int \delta K d\mathbf{v} \\ &= -f_t \frac{q_e n_{h0}}{T_{h0}} \left[ 2 \left( 1 - \frac{\omega_{*n,h}}{\omega} + \frac{3}{2} \frac{\omega_{*T,h}}{\omega} \right) \zeta R_1(\sqrt{\zeta}) \right. \\ &\quad \left. - 2 \frac{\omega_{*T,h}}{\omega} \zeta R_3(\sqrt{\zeta}) \right] (\delta\phi - \delta\psi) \\ &\quad - f_t \frac{q_e n_{h0}}{T_{h0}} \left[ 2 \left( 1 - \frac{\omega_{*n,h}}{\omega} + \frac{3}{2} \frac{\omega_{*T,h}}{\omega} \right) R_3(\sqrt{\zeta}) \right. \\ &\quad \left. - 2 \frac{\omega_{*T,h}}{\omega} R_5(\sqrt{\zeta}) \right] \delta\psi \end{aligned} \quad (21)$$

and

$$\begin{aligned} \delta P_h^{NA} &= \frac{1}{2} \int \delta K E d\mathbf{v} \\ &= -f_t q_e n_{h0} \left[ \left( 1 - \frac{\omega_{*n,h}}{\omega} + \frac{3}{2} \frac{\omega_{*T,h}}{\omega} \right) \zeta R_3(\sqrt{\zeta}) \right. \\ &\quad \left. - \frac{\omega_{*T,h}}{\omega} \zeta R_5(\sqrt{\zeta}) \right] (\delta\phi - \delta\psi), \quad (22) \\ &\quad - f_t q_e n_{h0} \left[ \left( 1 - \frac{\omega_{*n,h}}{\omega} + \frac{3}{2} \frac{\omega_{*T,h}}{\omega} \right) R_5(\sqrt{\zeta}) \right. \\ &\quad \left. - \frac{\omega_{*T,h}}{\omega} R_7(\sqrt{\zeta}) \right] \delta\psi \end{aligned}$$

where  $\zeta = \omega/\omega_{D0,h}$ , the response functions are given by

$$\begin{aligned} R_1(\sqrt{\zeta}) &= 1 + \sqrt{\zeta} Z(\sqrt{\zeta}), \\ R_3(\sqrt{\zeta}) &= \frac{1}{2} + \zeta + (\zeta)^{3/2} Z(\sqrt{\zeta}), \\ R_5(\sqrt{\zeta}) &= \frac{3}{4} + \frac{1}{2}\zeta + \zeta^2 + (\zeta)^{5/2} Z(\sqrt{\zeta}), \\ R_7(\sqrt{\zeta}) &= \frac{15}{8} + \frac{3}{4}\zeta + \frac{1}{2}\zeta^2 + \zeta^3 + (\zeta)^{7/2} Z(\sqrt{\zeta}), \end{aligned}$$

and  $Z(x) = \frac{1}{\sqrt{\pi}} \int_{-\infty}^{+\infty} \frac{\exp(-t^2)}{t-x} dt$  is the plasma dispersion function. Substituting equations (12)–(15), (17), (21) and (22) into equation (9), the non-adiabatic parallel velocity  $\delta u_{||h}^{NA}$  is readily solved as

$$\begin{aligned} \delta u_{||h}^{NA} &= -\frac{q_e}{T_{h0}} \frac{\omega}{k_{||}} (1 - f_t) \left( 1 - \frac{\omega_{*n,h}}{\omega} \right) (\delta\phi - \delta\psi) - 2 \frac{q_e}{T_{h0}} \frac{\omega}{k_{||}} \\ &\quad \times \left( \frac{\omega_{D,h}}{\omega} - f_t \frac{3}{4} \frac{\omega_{D0,h}}{\omega} \right) \left( 1 - \frac{\omega_{*n,h}}{\omega} - \frac{\omega_{*T,h}}{\omega} \right) \delta\psi, \end{aligned} \quad (23)$$

where  $\omega_{D,h} = -i \frac{cT_{h0}}{q_e B_0} \mathbf{b}_0 \times \boldsymbol{\kappa} \cdot \nabla$ . In the derivation of equation (23), the resonance terms associated with  $Z(\sqrt{\zeta})$  in equations (21) and (22) exactly cancel out with each other through equation (9), which again proves that the trapped EE particles do not carry parallel current as we assumed before. Note that  $\delta u_{||h}^{NA}$  can also be computed by integrating equation (7) in velocity space with passing EE fraction, which is consistent with equation (23) in the leading order.

### 2.3. Formulation of Landau-fluid bulk plasma and drift-kinetic EE hybrid model

Next, we couple the EE moments described by equations (12)–(15) and (21)–(23) to the bulk plasma Landau-fluid model in [25], and then yield the final fluid-kinetic hybrid model as follows. It should be pointed out that we use the electron charge symbol ‘ $q_e$ ’ in this work, while [25] uses the elementary charge symbol ‘ $e$ ’, which lead to the sign differences of some terms since  $q_e = -e$ .

$$\begin{aligned} & \left[ \frac{\partial}{\partial t} (1 + 0.75 \rho_i^2 \nabla_{\perp}^2) + i \omega_{*p,i} \right] \frac{c}{V_A^2} \nabla_{\perp}^2 \delta \phi \\ & + \mathbf{B}_0 \cdot \nabla \left( \frac{1}{B_0} \nabla_{\perp}^2 \delta A_{||} \right) - \frac{4\pi}{c} \boldsymbol{\delta B} \cdot \nabla \left( \frac{J_{||0}}{B_0} \right) \\ & - 8\pi (\nabla \delta P_i + \nabla \delta P_e) \cdot \frac{\mathbf{b}_0 \times \boldsymbol{\kappa}}{B_0} - \underbrace{8\pi \nabla \delta P_h^A \cdot \frac{\mathbf{b}_0 \times \boldsymbol{\kappa}}{B_0}}_{\{\text{EE-IC}\}} \\ & - i \frac{8\pi q_e}{c T_{h0}} \omega_{D0,h} \delta P_h^{NA} = 0, \end{aligned} \quad (24)$$

$$\begin{aligned} \frac{\partial \delta A_{||}}{\partial t} = & -c \mathbf{b}_0 \cdot \nabla \delta \phi - \frac{c T_{e0}}{q_e n_{e0}} \mathbf{b}_0 \cdot \nabla \delta n_e - \frac{c T_{e0}}{q_e n_{e0} B_0} \boldsymbol{\delta B} \cdot \nabla n_{e0} \\ & - \frac{c m_e}{q_e} \sqrt{\frac{\pi}{2}} v_{the} |k_{||}| \delta u_{||e} + \frac{c^2}{4\pi} \eta_{||} \nabla_{\perp}^2 \delta A_{||}, \end{aligned} \quad (25)$$

$$\begin{aligned} \frac{\partial \delta P_i}{\partial t} + \frac{c \mathbf{b}_0 \times \nabla \delta \phi}{B_0} \cdot \nabla P_{i0} + 2 \Gamma_{i\perp} P_{i0} c \nabla \delta \phi \cdot \frac{\mathbf{b}_0 \times \boldsymbol{\kappa}}{B_0} \\ + \Gamma_{i||} P_{i0} \mathbf{B}_0 \cdot \nabla \left( \frac{\delta u_{||i}}{B_0} \right) - i \Gamma_{i\perp} \omega_{*p,i} Z_i n_{i0} \rho_i^2 \nabla_{\perp}^2 \delta \phi \\ + 2 \Gamma_{i\perp} P_{i0} \frac{c}{Z_i} \nabla \delta T_i \cdot \frac{\mathbf{b}_0 \times \boldsymbol{\kappa}}{B_0} + 2 \Gamma_{i\perp} T_{i0} \frac{c}{Z_i} \nabla \delta P_i \cdot \frac{\mathbf{b}_0 \times \boldsymbol{\kappa}}{B_0} \\ + n_{i0} \frac{2}{\sqrt{\pi}} \sqrt{2} v_{thi} |k_{||}| \delta T_i = 0, \end{aligned} \quad (26)$$

$$\begin{aligned} m_i n_{i0} \frac{\partial \delta u_{||i}}{\partial t} = & \frac{Z_i n_{i0}}{q_e n_{e0}} \left( \mathbf{b}_0 \cdot \nabla \delta P_e + \frac{1}{B_0} \boldsymbol{\delta B} \cdot \nabla P_{e0} \right) \\ & - \left( \mathbf{b}_0 \cdot \nabla \delta P_i + \frac{1}{B_0} \boldsymbol{\delta B} \cdot \nabla P_{i0} \right) \\ & + Z_i n_{i0} \frac{m_e}{q_e} \sqrt{\frac{\pi}{2}} v_{the} |k_{||}| \delta u_{||e} - Z_i n_{i0} \frac{c}{4\pi} \eta_{||} \nabla_{\perp}^2 \delta A_{||}, \end{aligned} \quad (27)$$

$$\begin{aligned} \frac{\partial \delta n_i}{\partial t} + \frac{c \mathbf{b}_0 \times \nabla \delta \phi}{B_0} \cdot \nabla n_{i0} + 2 c n_{i0} \nabla \delta \phi \cdot \frac{\mathbf{b}_0 \times \boldsymbol{\kappa}}{B_0} \\ + n_{i0} \mathbf{B}_0 \cdot \nabla \left( \frac{\delta u_{||i}}{B_0} \right) - i \omega_{*p,i} \frac{Z_i n_{i0}}{T_{i0}} \rho_i^2 \nabla_{\perp}^2 \delta \phi \\ + \frac{2c}{Z_i} \nabla \delta P_i \cdot \frac{\mathbf{b}_0 \times \boldsymbol{\kappa}}{B_0} = 0, \end{aligned} \quad (28)$$

where  $\delta P_h^A = \delta P_{||h}^A = \delta P_{\perp h}^A$  in equation (24),  $Z_i n_{i0} + q_e (n_{e0} + n_{h0}) = 0$ , and the definitions of bulk plasma variables are consistent with [25]. The two-moment and three-moment Landau closures are applied to thermal electrons in equation (25) and thermal ions in equation (26) respectively, which show good agreements with drift-kinetic theory on the response functions in the regime of  $k_{||} v_{thi} \ll \omega \ll k_{||} v_{the}$  [32]. To close above equation set, we also have the equations for  $\delta P_e$ ,  $\delta T_e$  and  $\delta T_i$  as

$$\delta P_e = \delta n_e T_{e0} + n_{e0} \delta T_e, \quad (29)$$

$$\mathbf{b}_0 \cdot \nabla \delta T_e + \frac{1}{B_0} \boldsymbol{\delta B} \cdot \nabla T_{e0} = 0 \quad (30)$$

and

$$\delta T_i = \frac{1}{n_{i0}} (\delta P_i - \delta n_i T_{i0}). \quad (31)$$

Meanwhile, the thermal electron perturbed density  $\delta n_e$  and parallel velocity  $\delta u_{||e}$  in equations (24), (25) and (27) are calculated through the quasi-neutrality condition and parallel Ampere’s law as

$$\delta n_e = -\frac{Z_i}{q_e} \delta n_i - \frac{c^2}{4\pi q_e V_A^2} \nabla_{\perp}^2 \delta \phi - \underbrace{(\delta n_h^A + \delta n_h^{NA})}_{\{\text{EE-density}\}} \quad (32)$$

and

$$q_e n_{e0} \delta u_{||e} = -Z_i n_{i0} \delta u_{||i} - \frac{c}{4\pi} \nabla_{\perp}^2 \delta A_{||} - \underbrace{q_e n_{h0} \delta u_{||h}}_{\{\text{EE-current}\}}. \quad (33)$$

Equations (4), (12)–(15), (21)–(23) and (24)–(33) form a closed system for the fluid-kinetic hybrid simulation model as shown in figure 1. The main characteristics are briefly summarized here: first the well-circulating and deeply-trapped approximations used for the integrals of EE moments do not break the EE continuity equation; second the EE and bulk plasma are coupled through the quasi-neutrality condition, parallel Ampere’s law and vorticity equation in a non-perturbative manner (Note that non-perturbative here refers to solving the exact solution of nonlinear eigenmode equation in terms of  $\omega$ , rather than full-f simulations of plasma nonlinear systems (i.e. nonlinearities in terms of distribution and field perturbations) without separating equilibrium and perturbed distributions); third in equation (24) the EE-KPC term (i.e. EE kinetic particle compression) is responsible for the dissipative excitation of AEs, and the EE-IC term (i.e. EE interchange



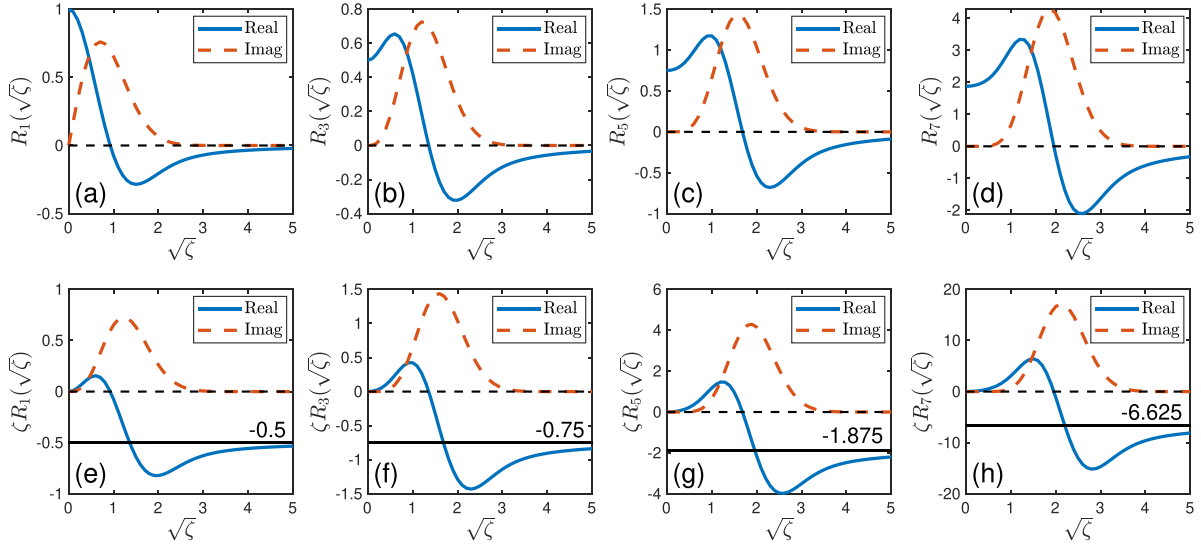


**Figure 2.** The real and imaginary parts of plasma response functions  $R_n(\sqrt{\zeta})$  and  $\zeta R_n(\sqrt{\zeta})$  in equations (21) and (22). The solid black lines with the numbers in (e)–(h) indicate the limit values at  $\zeta \rightarrow +\infty$ .

Since EE equilibrium pressure is comparable to thermal electron equilibrium pressure, we can define the smallness parameter  $\delta$

$$\delta \sim \frac{n_{h0}}{n_{e0}} \sim \frac{T_{e0}}{T_{h0}} \sim \epsilon^2 \ll 1, \quad (42)$$

where  $\epsilon = r/R_0$ . Note that  $L_{n,e} \sim L_{T,e} \sim L_{n,h} \sim L_{T,h}$  and  $L_{n,h}/L_{B,h} \sim \epsilon$  (where  $L_n = |\nabla \ln(n)|^{-1}$ ,  $L_T = |\nabla \ln(T)|^{-1}$  and  $L_B = |\nabla \ln(B)|^{-1}$  denote the scale lengths of plasma density and temperature, and magnetic field respectively), we have

$$\frac{\omega_{D,e}}{\omega_{D,h}} \sim \frac{\omega_{*,e}}{\omega_{*,h}} \sim \frac{\omega_{*,e}}{\omega_{*,h}} \sim \delta \quad (43)$$

and

$$\frac{\omega_{D,h}}{\omega_{*,h}} \sim \delta^{1/2}, \quad (44)$$

where  $\omega_{*,h} = \omega_{*,n,h} + \omega_{*,T,h}$ . Moreover, the EE precessional drift resonance requires

$$\omega \sim \omega_{D,h}. \quad (45)$$

Then the orders of EE moments can be estimated based on equations (42)–(45). In the electrostatic limit  $\delta\psi = 0$ , we have

$$\frac{\delta n_h^A}{\delta n_e} \sim \frac{n_{h0}}{n_{e0}} \frac{T_{e0}}{T_{h0}} \sim O(\delta^2), \quad (46)$$

$$\frac{\delta n_{h,0}^{NA}}{\delta n_e} = 0, \quad (47)$$

$$\frac{\delta n_{h,+ \infty}^{NA}}{\delta n_e} \sim -f_t \frac{n_{h0}}{n_{e0}} \frac{T_{e0}}{T_{h0}} \left(1 - \frac{\omega_{*,n,h}}{\omega}\right) \sim O(\delta^{3/2}), \quad (48)$$

$$\frac{n_{h0} \delta u_{||h}}{n_{e0} \delta u_{||e}} \sim (1 - f_t) \frac{n_{h0} T_{e0}}{n_{e0} T_{h0}} \left(\frac{\omega - \omega_{*,n,h}}{\omega - \omega_{*,n,e}}\right) \sim O(\delta^{3/2}), \quad (49)$$

$$\frac{\delta P_h^A}{\delta P_e} = \frac{n_{h0}}{n_{e0}} \sim O(\delta), \quad (50)$$

$$\frac{\delta P_{h,0}^{NA}}{\delta P_e} = 0 \quad (51)$$

and

$$\frac{\delta P_{h,+ \infty}^{NA}}{\delta P_e} \sim -\frac{3}{4} f_t \frac{n_{h0}}{n_{e0}} \left(1 - \frac{\omega_{*,n,h}}{\omega} - \frac{\omega_{*,T,h}}{\omega}\right) \sim O(\delta^{1/2}). \quad (52)$$

It is seen that only  $\delta P_h^{NA}$  is probably close to  $\delta P_e$  when  $\zeta \rightarrow \infty$ , however, the vorticity equation (24) that contains  $\delta P_h^{NA}$  term becomes redundant in the electrostatic limit, thus EEs are not important to the electrostatic polarized modes. In the electromagnetic limit  $\delta\phi = \delta\psi$ , we have

$$\frac{\delta n_h^A}{\delta n_e} \sim \frac{n_{h0}}{n_{e0}} \frac{T_{e0}}{T_{h0}} \frac{\omega_{*,n,h}}{\omega_{*,n,e}} \sim O(\delta), \quad (53)$$

$$\frac{\delta n_{h,0}^{NA}}{\delta n_e} \sim f_t \frac{n_{h0}}{n_{e0}} \frac{T_{e0}}{T_{h0}} \frac{\omega - \omega_{*,n,h}}{\omega_{*,n,e}} \sim O(\delta), \quad (54)$$

$$\frac{\delta n_{h,+ \infty}^{NA}}{\delta n_e} = 0, \quad (55)$$

$$\frac{n_{h0} \delta u_{||h}}{n_{e0} \delta u_{||e}} \sim \frac{n_{h0} T_{e0}}{n_{e0} T_{h0}} \left(\frac{\omega_{D,h} - \frac{3}{4} f_t \omega_{D0,h}}{\omega_{D,e}}\right) \times \left(\frac{\omega - \omega_{*,n,h} - \omega_{*,T,h}}{\omega - \omega_{*,n,e} - \omega_{*,T,e}}\right) \sim O(\delta^{1/2}), \quad (56)$$

$$\frac{\delta P_h^A}{\delta P_e} \sim \frac{n_{h0}}{n_{e0}} \left(\frac{\omega_{*,n,h} + \omega_{*,T,h}}{\omega_{*,n,e} + \omega_{*,T,e}}\right) \sim 1, \quad (57)$$

$$\frac{\delta P_{h,0}^{NA}}{\delta P_e} = 0 \quad (58)$$

and

$$\frac{\delta P_{h,+}^{NA}}{\delta P_e} \sim -\frac{3}{4} \frac{n_{h0}}{n_{e0}} \left( \frac{\omega_{*n,h} + \omega_{*T,h} - \omega}{\omega_{*n,e} + \omega_{*T,e}} \right) \sim 1. \quad (59)$$

Therefore,  $\delta P_h^A$ ,  $\delta P_h^{NA}$  and  $\delta u_{||h}$  are the leading order terms in the electromagnetic limit, and should be kept for EE species in the hybrid model, while the EE density perturbations  $\delta n_h^A$  and  $\delta n_h^{NA}$  can be safely dropped as higher order small terms.

#### 4. Verification and validation of upgraded MAS model with EE physics

The fluid-kinetic hybrid model in section 2.3 can be casted into a nonlinear eigenvalue equation in  $\omega$  as

$$\mathbb{A}\mathbf{X} - \omega\mathbb{B}\mathbf{X} + \mathbb{C}(\omega)\mathbf{X} = 0, \quad (60)$$

where  $\mathbb{A}$  and  $\mathbb{B}$  are the operators of bulk plasma Landau-fluid model and are independent of  $\omega$ , and  $\mathbb{C}(\omega)$  is the drift-kinetic EE operator that relies on  $\omega$  nonlinearly. We use Newton's iterative method to solve equation (60) with the initial guesses of  $(\omega, \mathbf{X})$  obtained from  $\mathbb{A}\mathbf{X} = \omega\mathbb{B}\mathbf{X}$ , which is efficient when EE term is small and perturbative. For cases that EE term is comparable with bulk plasma terms, we solve  $\mathbb{A}\mathbf{X} - \omega\mathbb{B}\mathbf{X} + \epsilon\mathbb{C}(\omega)\mathbf{X} = 0$  in the middle steps instead of directly solving equation (60), where  $\epsilon$  is an adjustable parameter that gradually increases from 0 to 1, thus the proper initial guesses of  $(\omega, \mathbf{X})$  can be obtained for each  $\epsilon$ -value case and guarantee the robustness of Newton's iterative method in the non-perturbative regime.

To verify the EE physics model and numerical scheme, we first validate the EE precession frequency that uses deeply-trapped approximation in both analytic and experimental tokamak geometries, and then carry out the verification simulations of e-BAE to demonstrate the correctness of EE precessional drift resonance.

##### 4.1. How good is deeply-trapped approximation for bounce-averaged guiding-center dynamics?

As claimed by equation (16) in section 2, we utilize the deeply-trapped approximation for calculating the precession frequency of trapped EE. To delineate its regime of validity, we compare equation (16) with the exact precession frequency by performing bounce average along the realistic banana orbit. The Boozer coordinates  $(\psi, \theta, \zeta)$  is applied in MAS to describe the magnetic field (where  $\psi$  is the poloidal magnetic flux,  $\theta$  and  $\zeta$  are the poloidal and toroidal Boozer angles respectively), which has the contravariant form  $\mathbf{B}_0 = q(\psi)\nabla\psi \times \nabla\theta - \nabla\psi \times \nabla\zeta$  and the covariant form  $\mathbf{B}_0 = I(\psi)\nabla\theta + g(\psi)\nabla\zeta$ . Then the guiding-center equation of motion in equilibrium  $B$ -field can be expressed in  $(\psi, \theta, \zeta)$  coordinates [33]

$$\dot{\psi} = -\frac{c}{Z_\alpha} \left( \frac{m_\alpha v_{||}^2}{B_0} + \mu \right) \frac{1}{JB_0^2} \left( g \frac{\partial B_0}{\partial \theta} \right), \quad (61)$$

$$\dot{\theta} = \frac{v_{||}}{JB_0} - \frac{cm_\alpha v_{||}^2}{Z_\alpha} \frac{1}{JB_0^2} \frac{\partial g}{\partial \psi} + \frac{c}{Z_\alpha} \left( \frac{m_\alpha v_{||}^2}{B_0} + \mu \right) \frac{1}{JB_0^2} g \frac{\partial B_0}{\partial \psi}, \quad (62)$$

$$\dot{\zeta} = \frac{qv_{||}}{JB_0} + \frac{cm_\alpha v_{||}^2}{Z_\alpha} \frac{1}{JB_0^2} \frac{\partial I}{\partial \psi} - \frac{c}{Z_\alpha} \left( \frac{m_\alpha v_{||}^2}{B_0} + \mu \right) \frac{1}{JB_0^2} I \frac{\partial B_0}{\partial \psi} \quad (63)$$

and

$$\dot{\rho}_{||} = -(1 - \rho_{||}g') \frac{c}{Z_\alpha} \left( \frac{m_\alpha v_{||}^2}{B_0} + \mu \right) \frac{1}{JB_0^2} \frac{\partial B_0}{\partial \theta}, \quad (64)$$

where  $\alpha$  denotes the particle species,  $J = (\nabla\psi \times \nabla\theta \cdot \nabla\zeta)^{-1}$  is the Jacobian and  $\rho_{||} = v_{||}/\Omega_{c\alpha}$ . Given energy  $E = 0.5v^2$  and pitch angle  $\lambda = \mu B_a / (m_\alpha E)$  of a particle, parallel velocity  $v_{||}$  can be written as

$$v_{||} = \pm \sqrt{2E \left( 1 - \lambda \frac{B_0}{B_a} \right)}, \quad (65)$$

and the bounce period can be calculated using equations (62) and (65) [33]

$$\tau_b = \oint d\theta / \dot{\theta} \simeq \oint \frac{JB_0}{v_{||}} d\theta. \quad (66)$$

Using equations (61)–(64) and (66), the exact precession frequency is then derived as [33]

$$\begin{aligned} \bar{\omega}_d &= \overline{n\mathbf{v}_d \cdot \nabla (\zeta - q\theta)} \\ &= \frac{n}{\tau_b} \left[ -\oint \frac{1}{\theta} \frac{c}{Z_\alpha} \left( \mu + \frac{m_\alpha v_{||}^2}{B_0} \right) \frac{\partial B_0}{\partial \psi} d\theta \right. \\ &\quad \left. + \oint \frac{cm_\alpha v_{||}}{Z_\alpha B_0} \left( \frac{\partial I}{\partial \psi} + q \frac{\partial g}{\partial \psi} \right) d\theta + \oint \rho_{||} g \frac{dq}{d\psi} d\theta \right] \end{aligned} \quad (67)$$

where  $n$  is the toroidal mode number, and the first term on the RHS is the leading order term that depends on both the radial  $\psi$  and poloidal  $\theta$  coordinates, i.e.  $\bar{\omega}_d = \bar{\omega}_d(\psi, \theta)$ .

The magnetic drift frequency  $\omega_d$  in Boozer coordinate can be expressed as

$$\begin{aligned} \omega_d &= -i\mathbf{v}_d \cdot \nabla = i \underbrace{\frac{c}{Z_\alpha} \left( \mu + \frac{m_\alpha v_{||}^2}{B_0} \right) \frac{1}{JB_0^2} \left[ g \frac{\partial B_0}{\partial \theta} \frac{\partial}{\partial \psi} \right]}_{\text{I}} \\ &\quad - n \underbrace{\frac{c}{Z_\alpha} \left( \mu + \frac{m_\alpha v_{||}^2}{B_0} \right) \frac{\partial B_0}{\partial \psi}}_{\text{II}} \\ &\quad + n \underbrace{\frac{cm_\alpha v_{||}^2}{Z_\alpha} \frac{1}{JB_0^2} \left( \frac{\partial g}{\partial \psi} q + \frac{\partial I}{\partial \psi} \right)}_{\text{III}} \end{aligned} \quad (68)$$

where term {I}, term {II} and term {III} represent the geodesic curvature, normal curvature and equilibrium current contributions respectively. In equation (68), we note that term {I} does

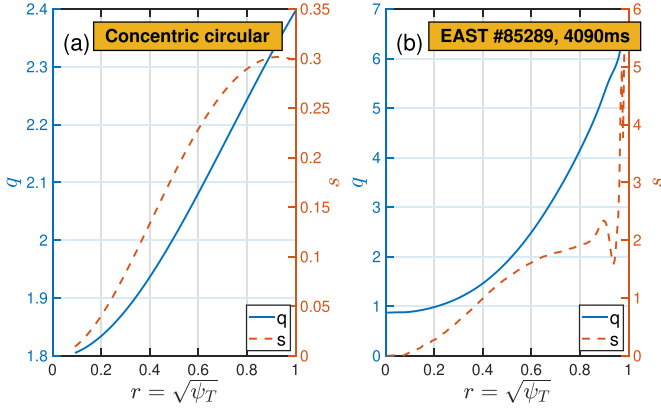


**Figure 3.** The safety factor  $q$  profile and magnetic shear  $s = \frac{r}{q} \frac{dq}{dr}$  profile in (a) analytic geometry and (b) experimental geometry of EAST discharge #85289 at 4090 ms.  $\psi_T$  is the normalized toroidal magnetic flux.

not contribute to the precession frequency since the geodesic drift cancels over a bounce period, effect of term {III} is ignorable, while term {II} is equal to equation (67) in the limit of  $\tau_b \rightarrow 0$ ,  $\theta \rightarrow 0$  and  $v_{||} \rightarrow 0$  (i.e. deeply-trapped limit)

$$\omega_{d0} = \bar{\omega}_{d, \tau_b \rightarrow 0} = -n \frac{c}{Z_\alpha} \left( \mu + \frac{m_\alpha v_{||}^2}{B_0} \right) \frac{\partial B_0}{\partial \psi} \Big|_{\theta=0}, \quad (69)$$

which is used for the deeply-trapped approximation in equation (16), and only has  $\psi$  dependence, i.e.  $\omega_{d0} = \omega_{d0}(\psi)$ .

In order to elucidate the accuracy of  $\omega_{d0}$ , we compare equations (67) and (69) in both the analytic geometry [17] and EAST experimental geometry [10]. The safety factor  $q$  and magnetic shear  $s = (r/q)(dq/dr)$  are given in figure 3. For analysis convenience, we use  $(\psi_{bc}, \theta_{tip})$  coordinates to represent trapped particles, where  $\psi_{bc} \in [0, \psi_{edge}]$  is the poloidal magnetic flux of banana orbit center and  $\theta_{tip} \in [0, 2\pi]$  is the Boozer poloidal angle at the banana tip location (i.e. the mirror throat). Using the magnetic field strength at  $(\psi_{bc}, \theta_{tip})$  location, i.e.  $B_{0,tip} = B_0(\psi_{bc}, \theta_{tip})$ , we can express the pitch angle of trapped particle as  $\lambda = B_a/B_{0,tip}$ , which varies in the range of  $B_a/B_{max} < \lambda < B_a/B_{min}$ . Substituting equation (65) into equation (67), the exact precession frequency  $\bar{\omega}_d$  can be calculated for all trapped particles in terms of  $(\psi_{bc}, \theta_{tip})$ . The ratio between  $\bar{\omega}_d(\psi_{bc}, \theta_{tip})$  and  $\omega_{d0}(\psi_{bc})$  in the analytic and EAST experimental geometries are shown in figures 4(a) and 5(a) respectively. First, it is seen that the numerical calculation of equation (67) agrees with the measurement from the realistic orbits by equations (61)–(64). Second, most areas on the low field sides are characterized with  $\bar{\omega}_d/\omega_{d0} \sim 1$ , thus  $\omega_{d0}$  in equation (69) can well approximate the precession frequency for most trapped particles not only in the analytic geometry with low magnetic shear but also in the experimental geometry with broader range of magnetic shear, where the significance of magnetic shear term in equation (67) is decreased by the elongation effect.

Moreover, since the trapped particle fraction  $f_t$  determines the EE drive intensity through equations (21) and (22), one

needs to adjust  $\lambda_{low}$  in equation (19) so that  $f_t$  only incorporates the contribution of trapped particles that satisfy  $\bar{\omega}_d/\omega_{d0} \sim 1$ , while the barely-trapped particles beyond the model capability should be excluded. Besides the constraint arising from the approximation on precession frequency, we note that the bounce average operations on electromagnetic fields in equation (8) are removed for integrating the EE moments, and corresponding validity regime of  $|\theta| \ll 1/|nq - m|$  becomes another constraint for  $\lambda_{low}$ . Figures 4(b) and 5(b) show the 2D profile of  $f_t$  using  $\lambda_{low} = B_a/B_{max}$  in the poloidal plane, which take into account all trapped particles and overestimate the deeply-trapped EE drive intensity. We then apply  $\lambda_{low} = 1$  in equation (19) to calculate  $f_t$  as shown in figures 4(c) and 5(c), which corresponds to the trapped particles with entire banana orbits on the low field side, in consistency with the validity regime of  $\bar{\omega}_d/\omega_{d0} \sim 1$  in figures 4(a) and 5(a). Thus, the 2D function  $f_t$  calculated by using  $\lambda_{low} = 1$  in equation (19) correctly reflects the deeply-trapped EE drive intensity for modes peak at  $k_{||} \sim 0$  and is applied in the following e-BAE simulations. For modes peak at moderate  $k_{||} \leq 1/qR_0$  such as e-TAE, one needs to choose  $\lambda_{low} < 1$  in equation (19) to calculate  $f_t$  in the more deeply-trapped regime (i.e. reduce  $\theta_b$ ). For comparison, the widely used simple 1D form of  $f_t \approx \sqrt{2\epsilon}$  assumes trapped particles distribute uniformly along the poloidal direction and might amplify the drive of deeply-trapped fraction. In addition, the omitted barely-trapped EE drive is in the higher order due to its small population.

#### 4.2. Comparison of e-BAEs between MAS model simulation and GTC gyrokinetic simulation

To verify the global fluid-kinetic hybrid simulation model and corresponding numerical implementation in MAS code, we carry out simulations of e-BAE in analytic geometry based on a well-established benchmark case [17], where the safety factor profile and concentric-circular geometry are shown in figures 3(a) and 4 respectively. Protons are used for thermal ions with  $Z_i = e$ . The thermal electron, thermal ion and EE temperatures are uniform with  $T_{i0} = T_{e0} = 500$  eV and  $T_{h0} = 25T_{e0}$ , and the thermal electron density is uniform with  $n_{e0} = 1.3 \times 10^{14} \text{ cm}^{-3}$ . The EE density profile is described by  $n_{h0} = 0.05n_{e0} \left[ 1 + 0.2 \left( \tanh \left( \frac{0.26 - \hat{\psi}}{0.06} \right) - 1.0 \right) \right]$ , where  $\hat{\psi} = \psi/\psi_w$  is the poloidal magnetic flux normalized by the wall value, and the reciprocal of EE density scale length  $R_0/L_{nh} = 12.7$  peaks at  $q=2$  rational surface, where  $L_{n,h} = (\nabla n_{h0}/n_{h0})^{-1}$ . The thermal ion density is then determined by the quasi-neutrality condition  $Z_i n_{i0} + q_e (n_{e0} + n_{h0}) = 0$ . The on-axis magnetic field strength is  $B_0 = 1.91$  T, the major radius is  $R_0 = 0.65$  m, the minor radius is  $a = 0.333R_0$ , and the safety factor profile in figure 3(a) is  $q = 1.797 + 0.8\hat{\psi} - 0.2\hat{\psi}^2$ . Note that  $\beta_h \sim \beta_e$  with these parameters, which is similar to fast ion pressure ordering for EI-driven AEs as shown in figure 3 of [34]. Nevertheless, here the EE density and temperature profiles are chosen for the dedicated benchmark study on e-BAE physics, and the EE- $\beta$  threshold for AE excitation can be given by simulation and theory, while it is still difficult to identify the exact EE distribution in experiments.

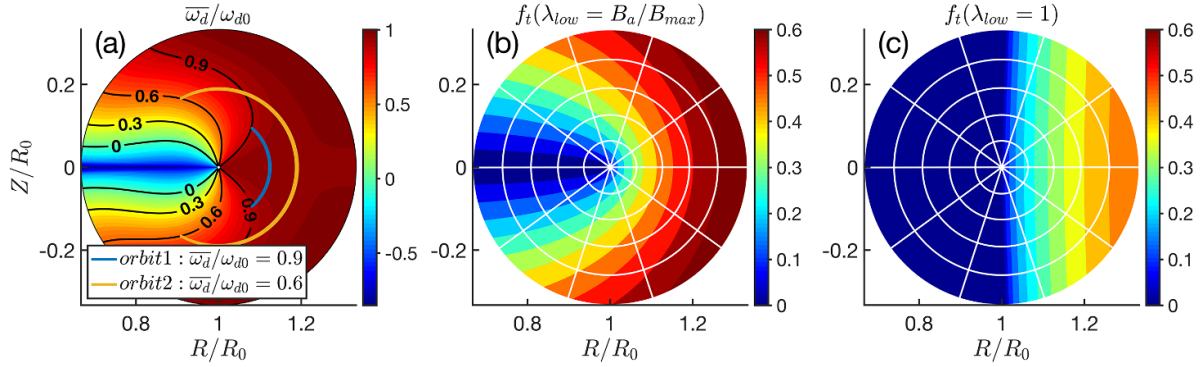


**Figure 4.** Analytic geometry using concentric circular. (a) The ratio between the exact precession frequency  $\bar{\omega}_d(\psi_{bc}, \theta_{tip})$  and the deeply-trapped approximation  $\omega_{d0}(\psi_{bc})$  of all trapped EEs in the poloidal plane. Note that  $\bar{\omega}_d/\omega_{d0}$  is plotted according to banana tip coordinates  $(\psi_{bc}, \theta_{tip})$ . The trapped particle fraction  $f_i$  in equation (19) with different lower cutoffs of pitch angle (b)  $\lambda_{low} = B_a/B_{max}$  and (c)  $\lambda_{low} = 1$ .

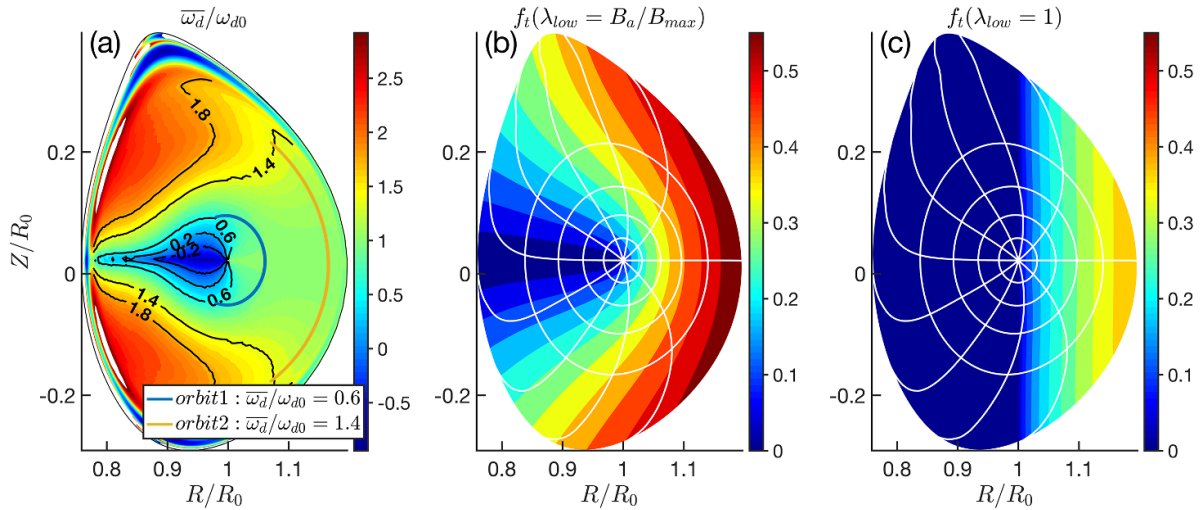


**Figure 5.** EAST geometry of discharge #85289 at 4090 ms. The captions of (a)–(c) are the same with figure 4.

The global mode structure and dispersion relation of  $n = 3$  e-BAE from MAS simulations using  $f_i(\lambda_{low} = 1)$  are analyzed as follows. The 2D poloidal mode structure of electrostatic potential  $\delta\phi$  is shown in figure 6(a1), which is characterized with a ‘boomerang’ shape. The dominant principal poloidal harmonic of  $m = 6$  peaks at  $q = 2$  rational surface, of which amplitude is much larger than the neighboring sideband harmonics of  $m = 5$  and  $m = 7$  that corresponds to a weakly ballooning structure as shown in figure 6(a2). Different from  $\delta\phi$ , the poloidal mode structure of parallel vector potential  $\delta A_{||}$  exhibits anti-ballooning feature as shown in figure 6(b1), where the real parts of  $m = 5$  and  $m = 7$  poloidal sidebands are comparable to the resonant  $m = 6$  harmonic but with phase difference as shown in figure 6(b2). Moreover, the mode structure of  $\Delta\phi = \delta\phi - \delta\psi$  is shown in figures 6(c1) and (c2), which represents the derivation from the ideal-MHD limit and reflects the polarization of each poloidal harmonics. The  $m = 6$  harmonic is predominantly Alfvénic according to the small  $\Delta\phi$  since the electrostatic component  $\delta\phi$  and electromagnetic component  $\delta\psi$  nearly cancel out, while  $\Delta\phi$  perturbation is large in  $m = 5$  and  $m = 7$  sidebands which indicates the acoustic component becomes more important.

It should be pointed out that there are ordering differences on constructing analytic equilibria between MAS and GTC early simulations in [17] though the parameter inputs are the same, and the EE mass ( $m_{EE}$ ) effect on e-BAE excitation is absent in [17] and awaits clarification. To investigate e-BAE physics in a more comprehensive way and careful benchmark MAS results, we carry out GTC simulations using current code version of GTC-4.6 with analytic equilibrium in the lowest order of inverse aspect ratio  $\epsilon = r/R_0$  described in appendix E of [35] that are identical to MAS simulations in figure 6. GTC results of e-BAE mode structure and wave-particle resonance are shown in figure 7 with scaling of EE mass  $m_{EE}/m_i$ , it is found that as  $m_{EE}/m_i$  decreases from 1/1 to realistic 1/1836, the  $\delta\phi$  2D mode structure exhibits a triangularity shape gradually, and the radial width of dominant  $m = 6$  harmonic becomes narrower indicated by the grey shaded region in figures 7(a2)–(d2). In GTC simulations, the wave-particle resonance strength can be inferred from the intensity of EE entropy  $\delta f_h^2$  in  $(E, \lambda)$  phase space as shown in figures 7(a3)–(d3), it is seen that the dominant EE resonance moves from bounce-precession near  $\lambda = 1$  to precession near  $\lambda = 1 + r/R_0 \approx 1.16$  as  $m_{EE}$  value decreases to the realistic

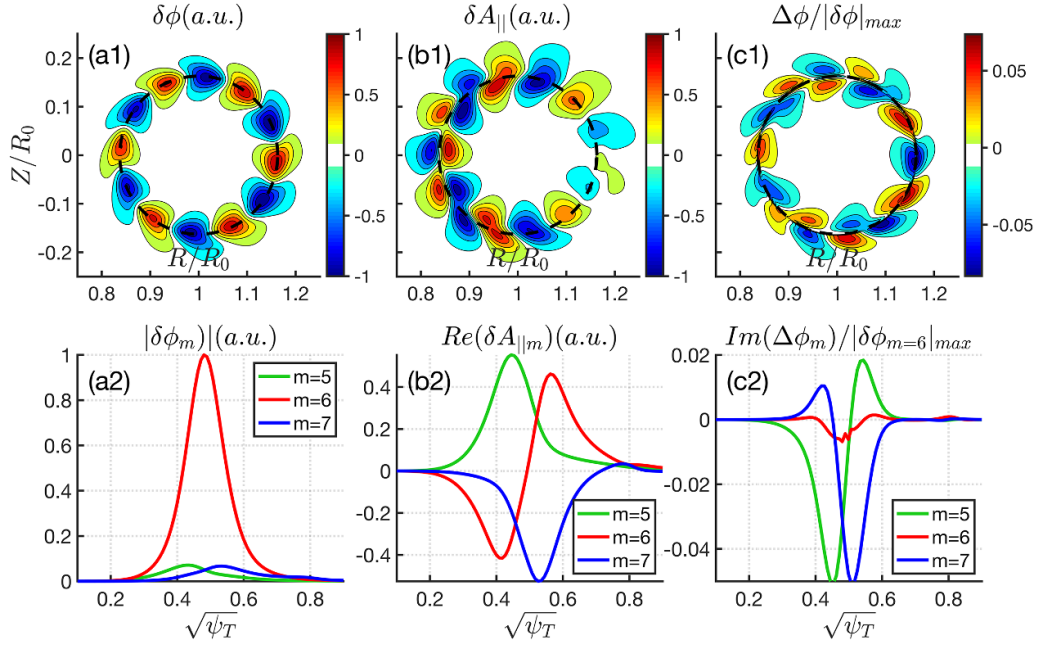


**Figure 6.** MAS simulation of  $n = 3$  e-BAE using  $f_i (\lambda_{low} = 1)$  and  $m_{EE}/m_i = 1/1836$  for EEs. The 2D poloidal mode structures of (a1) electrostatic potential  $\delta\phi$ , (b1) parallel vector potential  $\delta A_{||}$  and (c1)  $\Delta\phi = \delta\phi - \delta\psi$  with the on-axis  $n_{h0} = 0.05n_{e0}$  and  $T_{h0} = 25T_{e0}$ . (a2), (b2) and (c2) are the corresponding radial profiles of each poloidal harmonic.

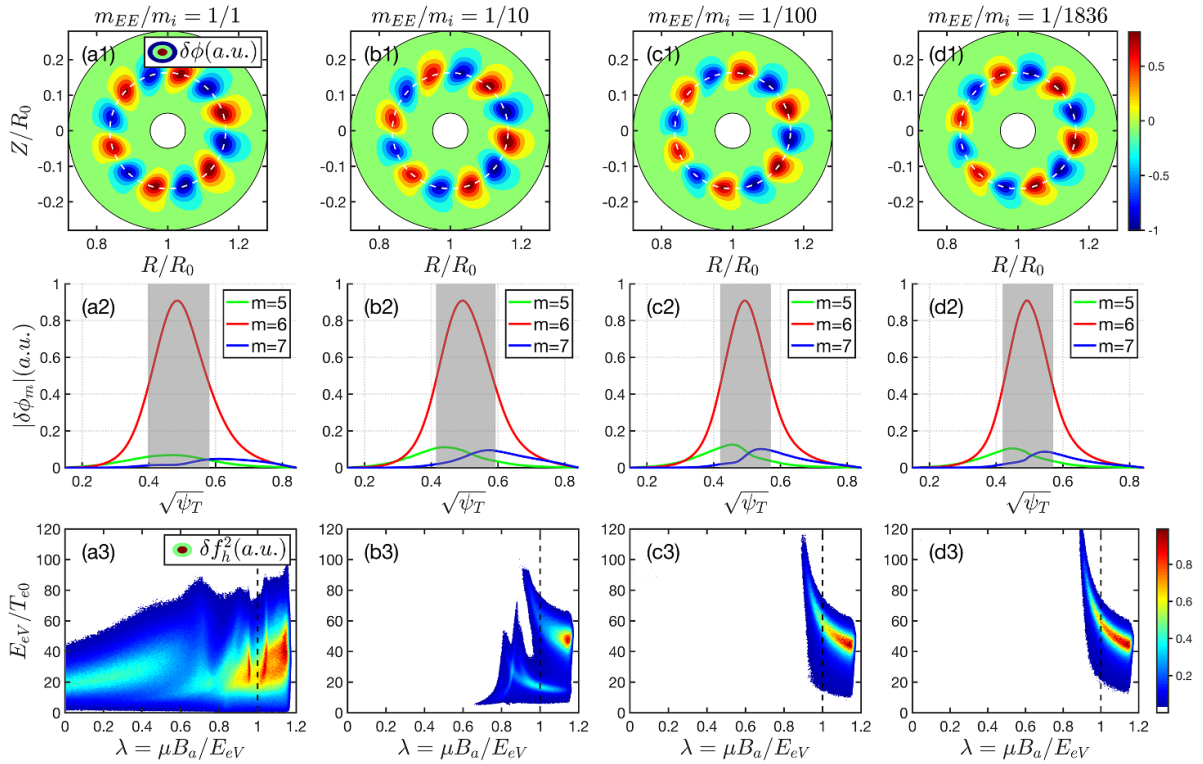


**Figure 7.** GTC simulation of  $n = 3$  e-BAE with different EE-ion mass ratios.  $m_{EE}/m_i = 1/1$ ,  $m_{EE}/m_i = 1/10$ ,  $m_{EE}/m_i = 1/100$  and  $m_{EE}/m_i = 1/1836$  are used from the left to the right column. The first row shows the 2D poloidal mode structures of  $\delta\phi$ , the middle row shows the radial profiles of each poloidal harmonic amplitude, and the bottom row shows the EE  $\delta f_h^2$  resonance structure in  $(E, \lambda)$  phase space. The grey shaded region indicates the full width at half maximum of dominant  $m = 6$  harmonic.

electron mass, which is consistent with recent theory that the bounce-averaged dynamics dominate EE resonances with low frequency MHD modes [13]. The corresponding e-BAE real frequency  $\omega_r$  and growth rate  $\gamma$  at different  $m_{EE}/m_i$  values

are shown in figure 8, it is noted that the variation of  $\omega_r$  is small which is mostly determined by bulk plasmas, however,  $\gamma$  of  $m_{EE}/m_i = 1$  case significantly deviates from other cases using smaller  $m_{EE}/m_i$  values, because the resonance region

in figure 7(a3) covers not only the precessional drift resonance but also the bounce-precession and transit resonances due to the unphysically large EE mass, while the resonance regions in figures 7(b3), (c3) and (d3) are dominated by precessional drift resonance and corresponding  $\gamma$  values are close with each other since trapped EE bounce-averaged dynamics only rely on temperature rather than mass [13]. Comparing the 2D mode structures and the 1D radial profiles of e-BAE  $m$ -harmonics between MAS simulation in figures 6(a1) and (a2) and GTC simulation in figures 7(d1) and (d2) using realistic  $m_{EE}/m_i = 1/1836$ , it is seen that MAS eigenvalue result mostly agrees with GTC PIC simulation on  $\delta\phi$  2D mode structure and corresponding radial profile of each  $m$ -harmonic. However, MAS gives relatively lower amplitudes of  $m = 5$  and  $m = 7$  sideband harmonics than GTC which reflects EE drive strength, because MAS applies deeply-trapped approximation for calculating EE drive in figure 6 using trapped fraction on the side of  $\lambda > \lambda_{low} = 1$ , while GTC simulation shows that a small part of  $\delta f_h^2$  resonance structure in phase space extends to the barely-trapped region on the side of  $\lambda < 1$  in figure 7(d3).

Regarding to the computational costs of MAS and GTC on e-BAE case above, MAS takes about 10 s with  $R = 100$  radial grids and  $M = 3$  coupled  $m$ -harmonics, and GTC runs 60 000 time steps by costing 55 GPU node hours on Perlmutter supercomputer (or 4000 CPU node hours) with  $m_{psi} = 128$ ,  $m_{theta} = 512$  and  $m_{toroidal} = 32$  grids in the radial, poloidal and parallel directions and 75 particles per grid-cell by summing all species. The huge computational cost of GTC is caused by the smallness of realistic EE mass, resulting in the stringent restriction on time step by EE parallel transit time (i.e.  $k_{||}v_{th,e}\Delta t \leq 1$ ) for initial value simulations [21]. The upgraded MAS code greatly improves the computational efficiency for modeling EE effects on low frequency MHD modes with  $\omega \ll \Omega_{ci}$ , which is useful for analyzing experimental observations and preparing data for training surrogate models in machine learning [36].

Next, we investigate parametric dependencies of e-BAE  $\omega_r$  and  $\gamma$  on EE drive, namely, compare MAS and GTC results by varying  $n_{h0}$  and  $T_{h0}$  in amplitudes while remaining profiles unchanged. Considering the EE  $\delta f_h^2$  resonance region in figure 7(d3) from GTC simulation, we perform MAS simulations with both  $\lambda_{low} = 1$  and  $\lambda_{low} = B_a/B_{max}$  as the lower limits of pitch angle for trapped fraction  $f_t$  calculations using equation (19). From figures 9(a) and (b), it is seen that  $\omega_r$  decreases and  $\gamma$  increases as  $n_{h0}/n_{e0}$  varies from 0 to 0.1 in both MAS and GTC simulations. Specifically, MAS results using  $\lambda_{low} = 1$  agree with GTC results near the marginal stable regime of small  $n_{h0}/n_{e0}$ , and MAS results using  $\lambda_{low} = B_a/B_{max}$  get close to GTC results as  $n_{h0}/n_{e0}$  increases. The reason can be explained by comparing GTC  $\delta f_h^2$  resonance regions in phase space between figures 9(c)–(e). For the weak EE drive case of  $n_{h0}/n_{e0} = 0.03$ , most intensity of  $\delta f_h^2$  distributes on the side of  $\lambda > 1$  where the deeply-trapped EE model using  $\lambda_{low} = 1$  can well approximate EE drive. However, the GTC  $\delta f_h^2$  resonance regions gradually extend to  $\lambda < 1$  side as  $n_{h0}/n_{e0}$  increases, and the realistic EE drive is then underestimated in MAS using  $\lambda_{low} = 1$ . On the other hand, MAS simulations using  $\lambda_{low} = B_a/B_{max}$  overestimate EE drive that

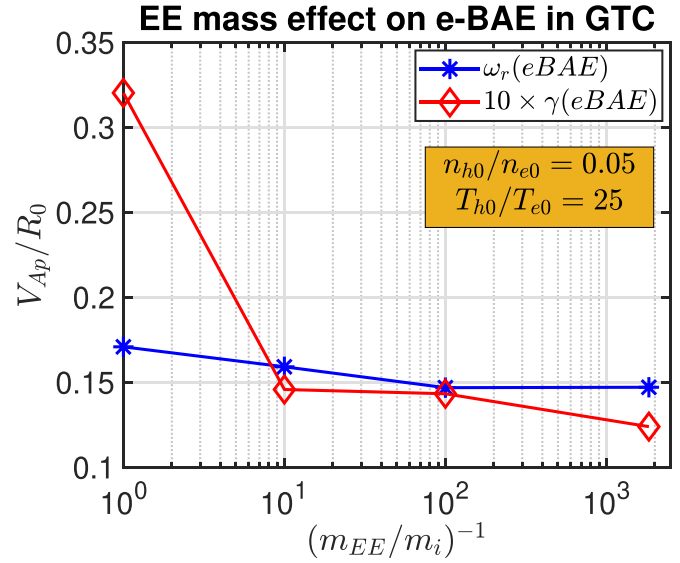


**Figure 8.** The real frequency  $\omega_r$  and growth rate  $\gamma$  of  $n = 3$  e-BAE using different  $m_{EE}/m_i$  values in GTC.

give higher  $\gamma$  than GTC because all trapped EEs are treated as deeply-trapped ones with precessional drift frequency that closely matches with the mode frequency. Similar conclusions are obtained for  $T_{h0}/T_{e0}$  scan as shown in figure 10. It should be pointed out that the ellipticity-induced AE (EAE) can be excited by EEs and grows faster than e-BAE in GTC initial value simulations when  $T_{h0}/T_{e0} \geq 40$ , thus we cannot measure corresponding GTC results of e-BAE  $\omega_r$  and  $\gamma$  for cases with  $T_{h0}/T_{e0} \geq 40$  in figure 10(b). It is also seen that the GTC results of  $\gamma$  exhibit a transition from MAS results using  $\lambda_{low} = 1$  to  $\lambda_{low} = B_a/B_{max}$  as  $T_{h0}/T_{e0}$  increases in figure 10(b). The intersections of the black dashed lines and growth rate curves in figures 9 and 10(a), (b) indicate the excitation thresholds that EE drive just overcomes the continuum damping [37, 38] and radiative damping/Landau damping from bulk plasma [39–41], and it is clear that MAS model using  $\lambda_{low} = 1$  is sufficient for estimating these excitation thresholds, where the deeply-trapped EE play a dominant role in the marginal stable regime. In a short summary, MAS model considers the precessional drift resonance as the dominant EE resonance with AEs, which is appropriate and confirmed by GTC PIC simulations using e-BAE as an example. It is also worthy mentioning that these EE-driven AE processes have similarities with alpha particle driven AEs in future fusion reactor, of which EP orbits and wave-particle resonances are numerically investigated and compared in appendix A.

#### 4.3. Non-perturbative analysis of BAE stability in presence of EE drive and bulk plasma damping

The symmetry breaking of AE mode structure due to non-ideal MHD effects, such as kinetic EPs induced anti-Hermitian part of dielectric tensor [42], have been widely observed in simulations [43, 44] and experiments [45, 46], which are characterized with twisted mode structures. Since the distortion of AE mode structure by EEs is much less explored compared

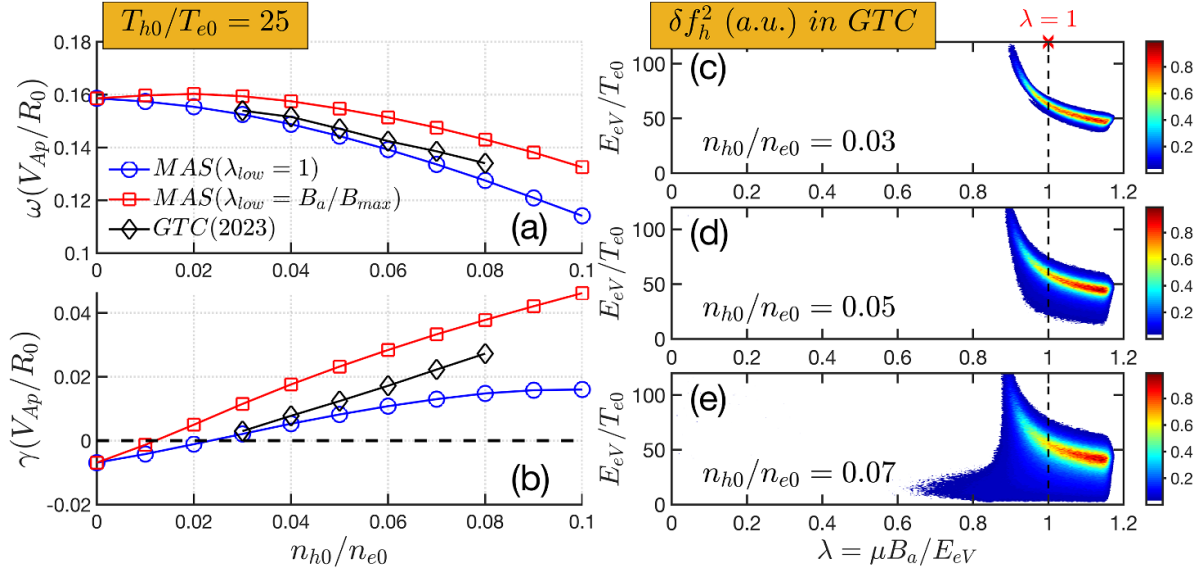


**Figure 9.** The comparisons of e-BAE real frequency  $\omega_r$  and growth rate  $\gamma$  between MAS (blue and red colors) and GTC (black color) simulations. (a)  $\omega_r$  and (b)  $\gamma$  dependences on EE density  $n_{h0}$  with fixed  $T_{h0} = 25T_{e0}$ . (c)–(e) show the resonance structures of EE entropy  $\delta f_h^2$  in  $(E, \lambda)$  phase space at different  $n_{h0}/n_{e0}$  values, and the dashed line indicates  $\lambda = 1$  boundary.

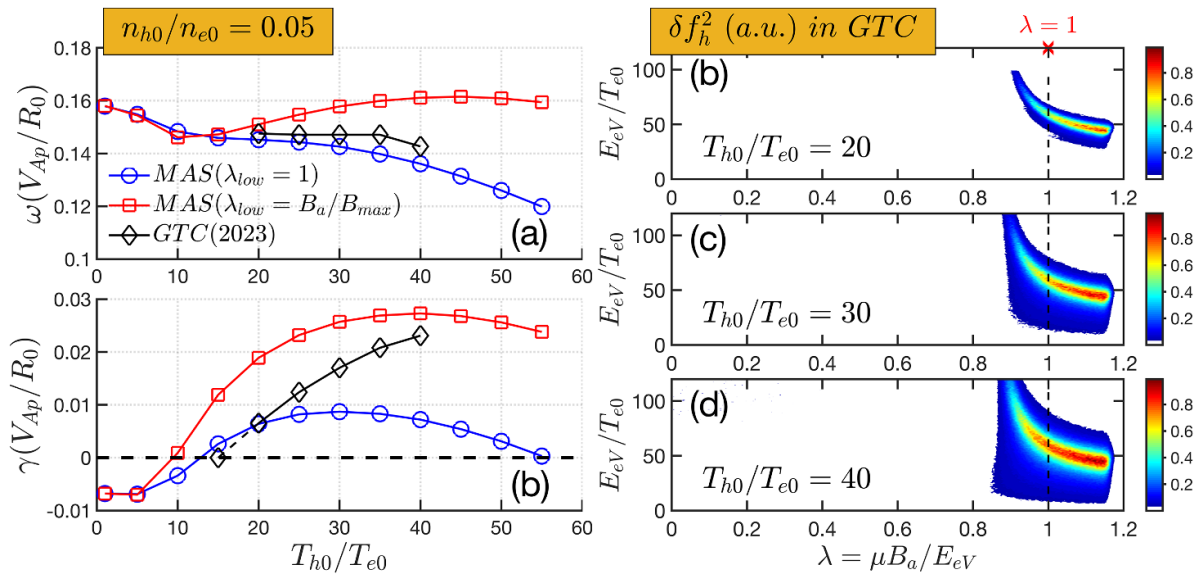


**Figure 10.** The comparisons of e-BAE real frequency  $\omega_r$  and growth rate  $\gamma$  between MAS (blue and red colors) and GTC (black color) simulations. (a)  $\omega_r$  and (b)  $\gamma$  dependences on EE temperature  $T_{h0}$  with fixed  $n_{h0} = 0.05n_{e0}$ . (c)–(e) show the resonance structures of EE entropy  $\delta f_h^2$  in  $(E, \lambda)$  phase space at different  $T_{h0}/T_{e0}$  values, and the dashed line indicates  $\lambda = 1$  boundary.

to EIs in experiments, we also perform GTC first-principle simulations of i-BAEs in appendix B to check the symmetry property between i-BAE and e-BAE. By comparing the mode structures of i-BAE in figure 19 and e-BAE in figure 7, the main difference is the tip orientation of ‘boomerang’ (triangularity) shape, and it can be speculated that the underlying physics of EE non-perturbative effects on BAE mode structure is similar to EIs except for negative charge sign and small FOWs. To understand the role of EEs on ‘boomerang’ (triangularity) shape mode structure in figure 6(a) that is no longer up-down symmetric, four MAS simulation cases are performed with different EE physics as described in table 1. Case {I} corresponds

to the Landau-fluid simulation of bulk plasma without any EE effects, and the poloidal mode structure is relatively up-down symmetric as shown in figure 11(aI), where the small distortion is due to the kinetic effects of bulk plasmas that lead to anti-Hermitian contribution. In case {II}, the EE-KPC term is added on top of case {I}, and the 2D mode structure is radially broadened and drastically twisted with obvious tails on both sides of mode rational surface in figure 11(bI), which indicates that the anti-Hermitian contribution from EE-KPC is much larger than bulk plasmas. For comparison, figure 11(cI) shows the 2D mode structure of case {III} that includes EE-IC term on top of case {I} instead of EE-KPC term, and it

**Table 1.** Four simulation cases of  $n = 3$  e-BAE with different EE physics. Note that EE-IC and EE-KPC terms are given in equation (24), which represent the fluid and kinetic EE responses respectively.

Case	EE-IC	EE-KPC	$\omega_r (V_{Ap}/R_0)$	$\gamma (V_{Ap}/R_0)$
(I)	No	No	0.160	-0.007 07
(II)	No	Yes	0.175	0.004 96
(III)	Yes	No	0.134	-0.009 09
(IV)	Yes	Yes	0.149	0.009 04

can be seen that EE-IC term has little impact on the symmetry breaking which is different from case {II}, but EE-IC term can broaden the radial width to a certain extent. In case {IV}, the non-perturbative effects of both EE-IC and EE-KPC terms are considered (figure 11(dI)), it is seen that the degree of symmetry breaking in case {IV} is between case {II} and case {III}, and the radial width is close to both case {II} and case {III}. Thus, there are two EE non-perturbative effects on e-BAE mode structure: (i) the EE-KPC term provides the dominant kinetic effects and induces the large anti-Hermitian part of dispersion relation, which is responsible for the distortion e-BAE mode structure; (ii) the EE-IC term represents the fluid-like convective response and enhances the Hermitian part, which not only compensates the symmetry breaking induced by EE-KPC term but also broadens the radial width through MHD interchange effect.

The radial profile of phase angle  $\theta_r$  can also reflect the mode structure symmetry, which has received interest from recent experiments [45, 46]. Here we combine  $\theta_r$  radial profiles of cases {I}–{IV} with corresponding 2D mode structures to illustrate their underlying connections. Since the poloidal harmonics of e-BAE are weakly coupled, we choose the dominant  $m = 6$  harmonic of  $\delta\phi$  and calculate  $\theta_r$  according to  $\delta\phi_{m=6} = |\delta\phi_{m=6}| \exp(i\theta_r)$ . In figure 12, the blue solid line represents  $\theta_r$ , the red solid and red dashed lines represent the real and imaginary parts of  $\delta\phi_{m=6}$  respectively, and the radial domain of e-BAE eigenfunction with finite amplitude is marked as a gray shaded region. As shown in figures 12(a) and (c),  $\theta_r$  profiles almost remain constant in the e-BAE region of cases {I} and {III}, which correspond to the relatively symmetric mode structures in figures 11(aI) and (cI) respectively. In contrast,  $\theta_r$  profiles show large variations in the e-BAE region of cases {II} and {IV} due to the anti-Hermitian EE-KPC term that breaks the poloidal up-down symmetry. However, the poloidal phase shifts at different radial locations are approximately symmetric with respect to the e-BAE peak as shown in figures 12(b) and (d) (because the EE gradient profile peaks at the mode rational surface in our simulations), which still indicate the radial symmetry of ‘boomerang’ shape mode structures characterized with two symmetric tails as shown in figures 11(bI) and (dI). In addition, we show the real frequencies, radial positions and mode widths of cases {I}–{IV} on corresponding  $n = 3$  continuous spectra in figure 13, where the Alfvénic and acoustic continua are calculated in MAS code based on an ideal full-MHD model as described in appendix B of [25].

Further, in order to clarify the competition between EE excitation and bulk plasma damping, we compute the EE drive  $\gamma_{\text{drive}}$  in the absence of dissipation by dropping Landau damping terms associated to  $|k_{\parallel}|$  in equations (25)–(27), and compute the bulk plasma damping rate  $\gamma_{\text{damp}}$  by isolating EE drive effect (i.e. only keeping the real part of EE response functions in equations (21) and (22) while dropping the imaginary part), and  $\gamma_{\text{drive}}$  and  $\gamma_{\text{damp}}$  dependencies on  $n_{h0}$  and  $T_{h0}$  are shown in figure 14 for EE trapped fraction  $f_t$  calculated with both  $\lambda_{\text{low}} = 1$  and  $\lambda_{\text{low}} = B_a/B_{\text{max}}$ . It should be noted that both bulk plasma and EE non-perturbative effects, namely, modifications on mode structure and real frequency, are kept for calculating  $\gamma_{\text{drive}}$  and/or  $\gamma_{\text{damp}}$ . For example,  $\gamma_{\text{damp}}$  shows relatively strong dependency on  $T_{h0}$  in figure 14(b), which indicates that EE non-perturbative effect can quantitatively affect the bulk plasma damping on e-BAE through altering the mode structure and real frequency, and thus becomes necessary for accurate damping and growth rate calculation. Readers may also notice that the change of  $\gamma_{\text{damp}}$  by varying  $T_{h0}$  becomes weaker in figure 14(d), the reason can be understood as follows. We recall that the EE-IC term incorporates both passing and trapped EE contributions (i.e., adiabatic fluid convection) in MAS model, while  $f_t$  only acts on EE-KPC term in equation (24), and the non-perturbative corrections on real frequency are opposite in sign between EE-IC term and EE-KPC term as illustrated in figure 13, thus larger  $f_t$  using  $\lambda_{\text{low}} = B_a/B_{\text{max}}$  in figure 14(d) gives rise to a larger cancellation of EE non-perturbative effect on real frequency, and the resonance condition for damping is less altered. Meanwhile, the  $\gamma_{\text{drive}} - |\gamma_{\text{damp}}|$  agrees well with the gross growth rate  $\gamma$  using comprehensive model with both EE drive and bulk plasma damping, which confirms the correctness of our method for obtaining  $\gamma_{\text{drive}}$  and  $\gamma_{\text{damp}}$  that covers not only the unstable regime of  $|\gamma_{\text{damp}}| \ll \gamma_{\text{drive}}$  but also the marginally stable regime of  $|\gamma_{\text{damp}}| \sim \gamma_{\text{drive}}$ , and thus provides useful damping and drive information for linear stability and further nonlinear dynamics analyses [47].

Finally, we present MAS simulation of e-BAEs in experimental geometry based on EAST discharge #82589 at 4090 ms, of which q profile and magnetic geometry are shown in figures 3(b) and 5. Within the ECRH and LHCD in EAST tokamak, multiple AEs with toroidal mode numbers  $n = 1$  and  $n = 2$  propagating along electron diamagnetic drift direction are observed in a wide frequency range of [20 kHz, 300 kHz]. Meanwhile, the EE population is enhanced during these AE activities based on the diagnosis of hard x-ray photon counts. Since EI effect is ignorable without applying ion cyclotron resonance heating (ICRH) and neutral-beam injection (NBI), the AEs in this EAST discharge are destabilized by EEs as reported in [10]. The thermal plasma profiles and corresponding Alfvén continua are shown in figures 6 and 7 of [10], here we focus on  $(m/n) = (4/1)$  BAE mode and analyze its stability in  $n_{h0} - T_{h0}$  space, the EE density profile is nonuniform given by  $n_{h0} = C \times n_{e0,a} \left[ 1 + 0.3 \left( \tanh \left( \frac{0.85 - \psi}{0.06} \right) - 1.0 \right) \right]$ , where  $C \ll 1$  is a constant and  $n_{e0,a}$  represents the thermal electron density at magnetic axis, and the EE temperature profile  $T_{h0}$  is uniform.

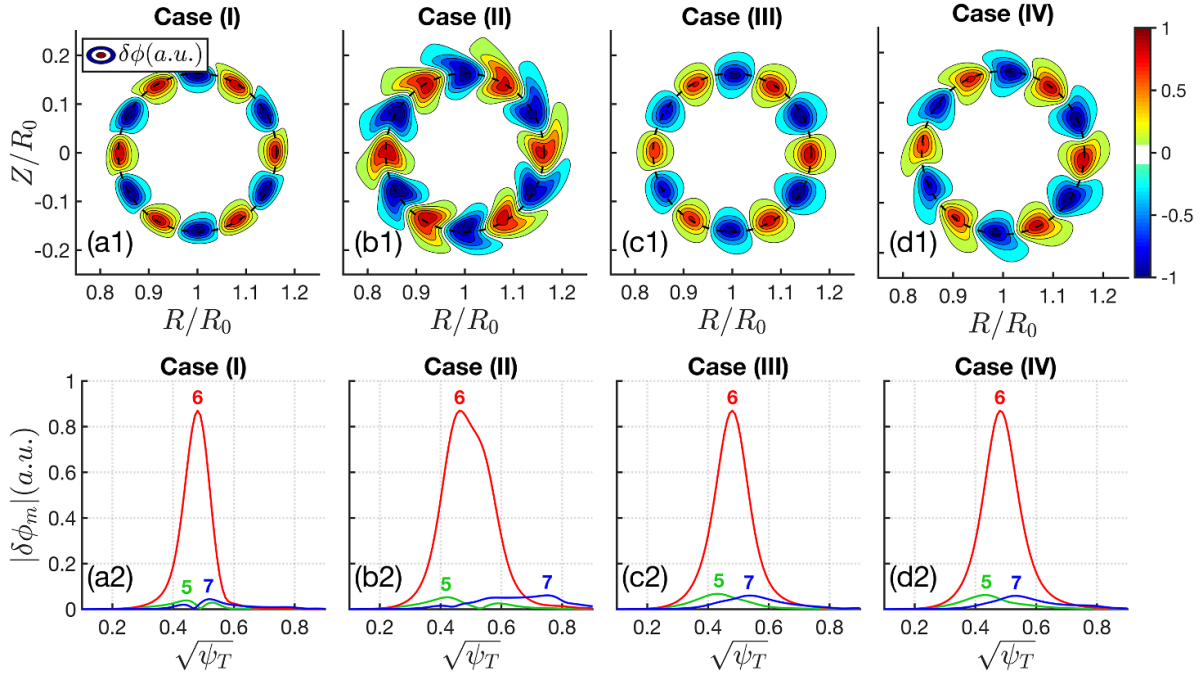


**Figure 11.** The 2D poloidal mode structures of electrostatic potential  $\delta\phi$  with different EE terms in equation (24) in MAS simulations. (a) Case (I): drop both EE-IC and EE-KPC terms. (b) Case (II): drop EE-IC term and keep EE-KPC term. (c) Case (III): keep EE-IC term and drop EE-KPC term. (d) Case (IV): keep both EE-IC and EE-KPC terms.

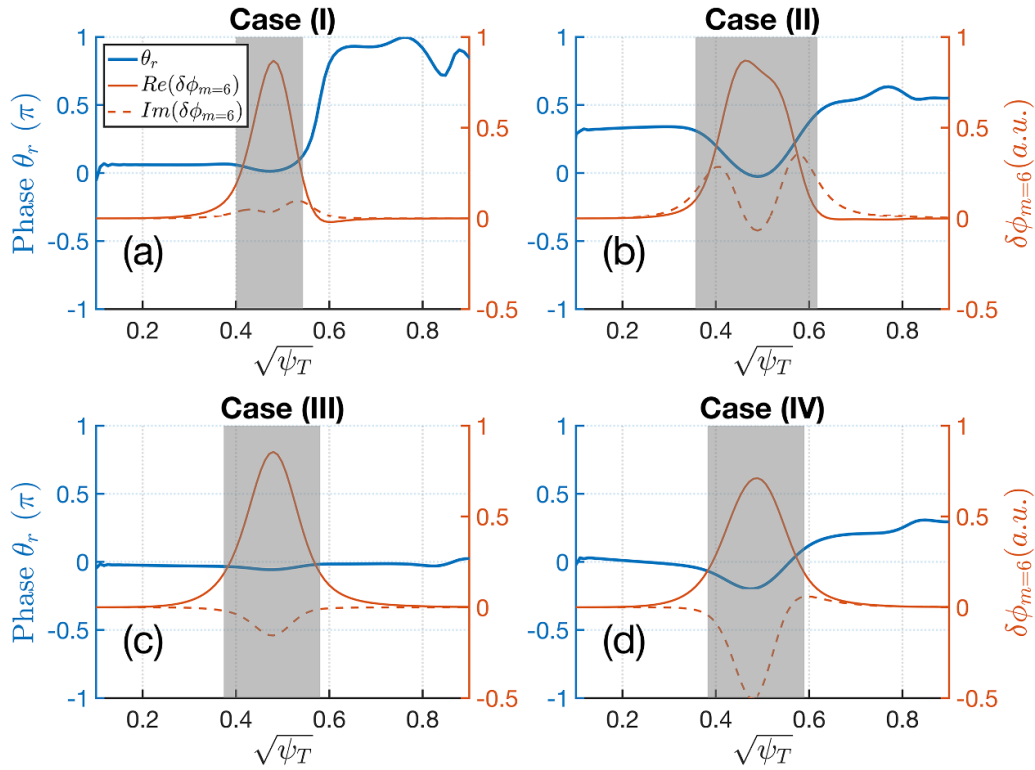


**Figure 12.** (a)–(d) The dominant  $m = 6$  harmonic radial profiles of electrostatic potential  $\delta\phi$  and corresponding phase angle  $\theta_r$  for cases (I)–(IV) in MAS. The radial profile of  $\theta_r = \arctan(\text{Im}(\delta\phi_{m=6})/\text{Re}(\delta\phi_{m=6}))$  is indicated by the blue solid line, and the radial profiles of  $\text{Re}(\delta\phi_{m=6})$  and  $\text{Im}(\delta\phi_{m=6})$  are indicated by the red solid line and red dashed line respectively. The gray shaded region indicates the radial domain of  $\delta\phi_{m=6}$  with high intensity.

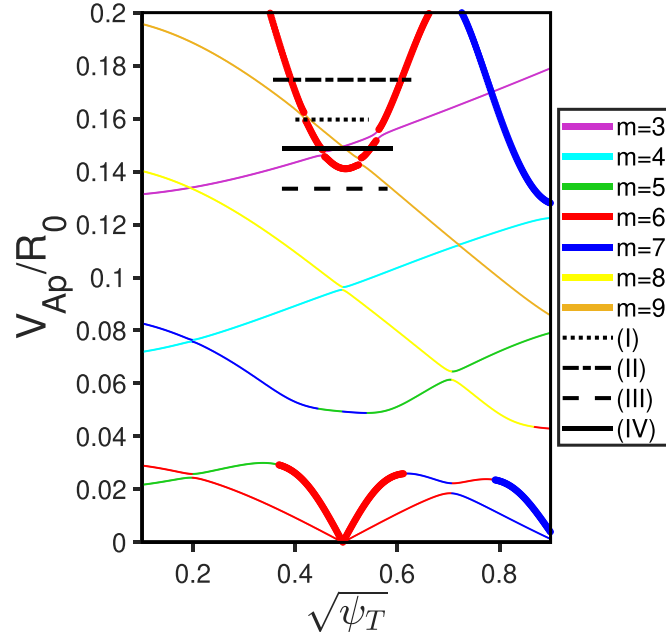


**Figure 13.** The e-BAE frequencies of cases (I)–(IV) and continuous spectra in MAS. The thick lines represent the Alfvénic branch and the thin lines represent the acoustic branch.

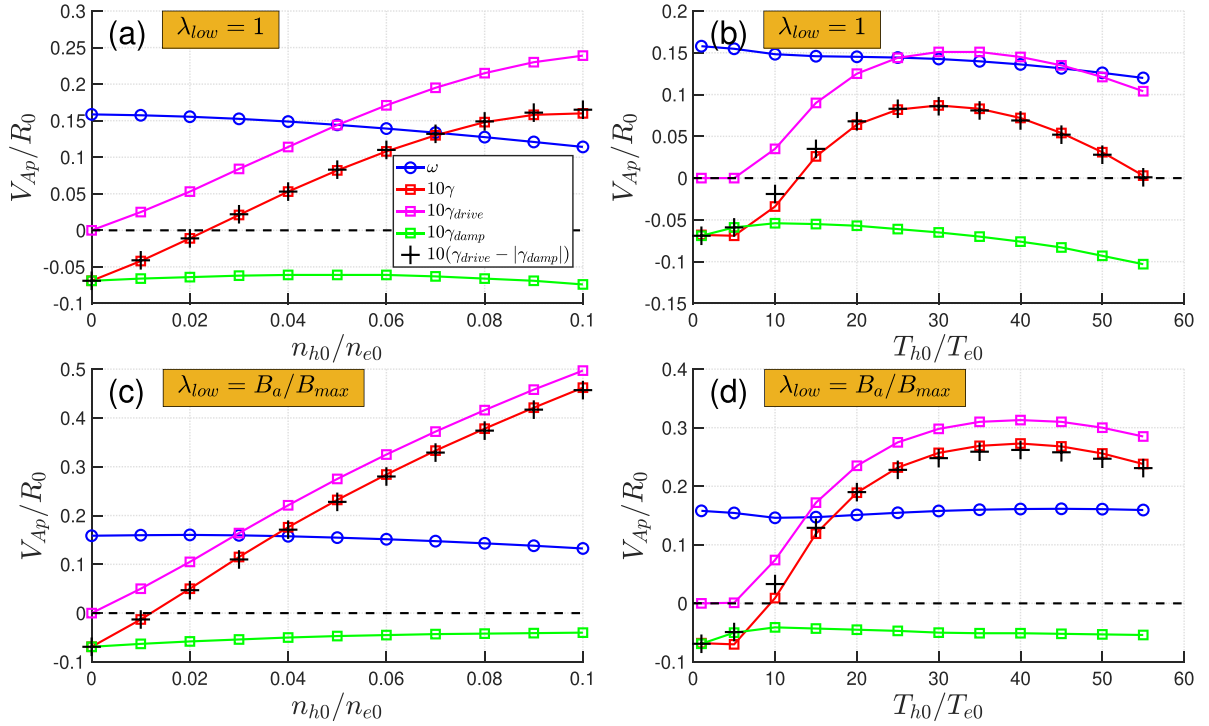


**Figure 14.** The kinetic EE drive  $\gamma_{drive}$  (the magenta squares) and bulk plasma damping  $\gamma_{damp}$  (the green squares) calculated by MAS. (a) and (c)  $n_{h0}$  scans with fixed  $T_{h0} = 25T_{e0}$ . (b) and (d)  $T_{h0}$  scans with fixed  $n_{h0} = 0.05n_{e0}$ . (a), (b)  $\lambda_{low} = 1$  in equation (19); (c), (d)  $\lambda_{low} = B_a/B_{max}$  in equation (19). The individual calculations of  $\gamma_{drive}$  and  $\gamma_{damp}$  are consistent with the gross growth rate  $\gamma$  (the red squares) obtained from simulations that incorporate both EE drive and bulk plasma damping.

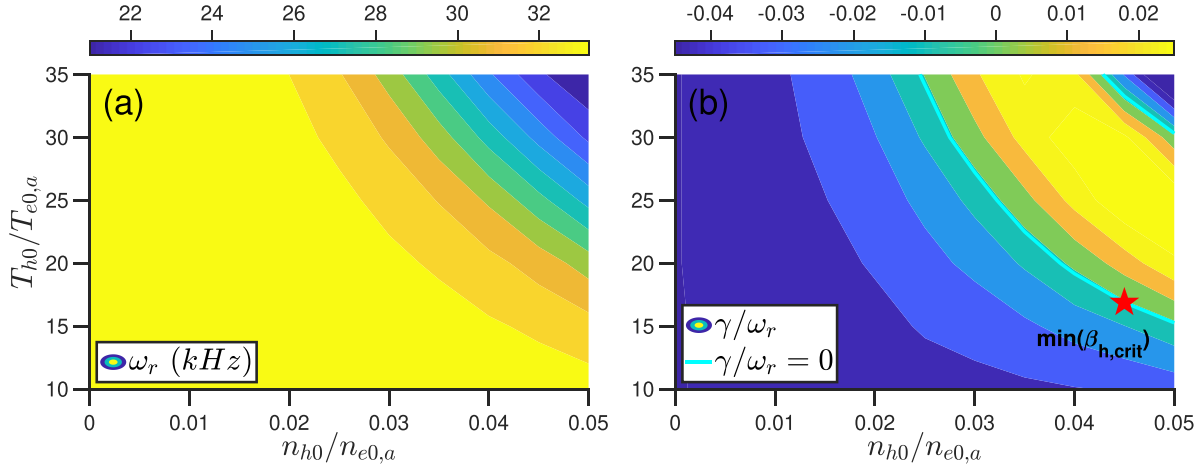


**Figure 15.** MAS simulation of  $m/n = 4/1$  e-BAE stability in EAST discharge #85289 at 4090 ms. (a)  $\omega_r$  and (b)  $\gamma$  dependencies on EE density  $n_{h0}$  and temperature  $T_{h0}$ . Cyan solid line represents the stability boundary of e-BAEs characterized by  $\gamma/\omega_r = 0$ , and red pentagram marks the  $(n_{h0}, T_{h0})$  location of the minimal EE- $\beta_h$  value required for e-BAE excitation.

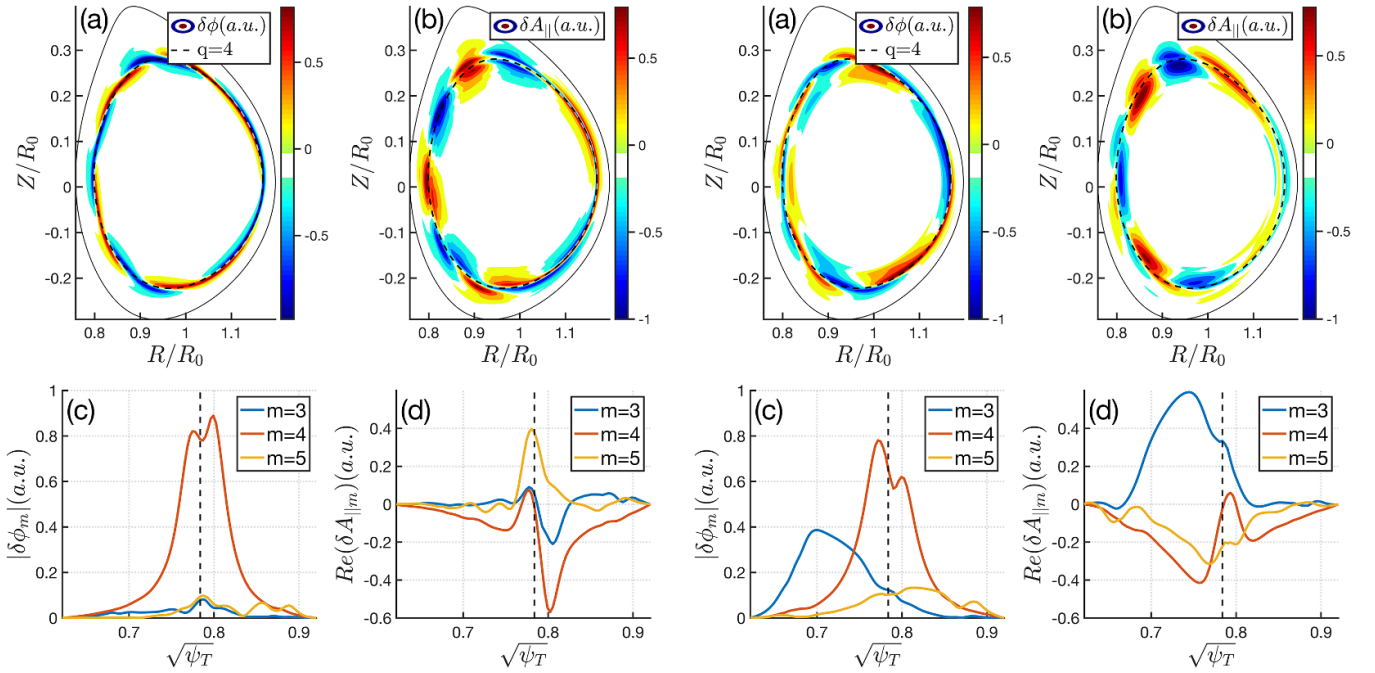


**Figure 16.**  $m/n = 4/1$  BAE mode structure in the absence of EE drive.

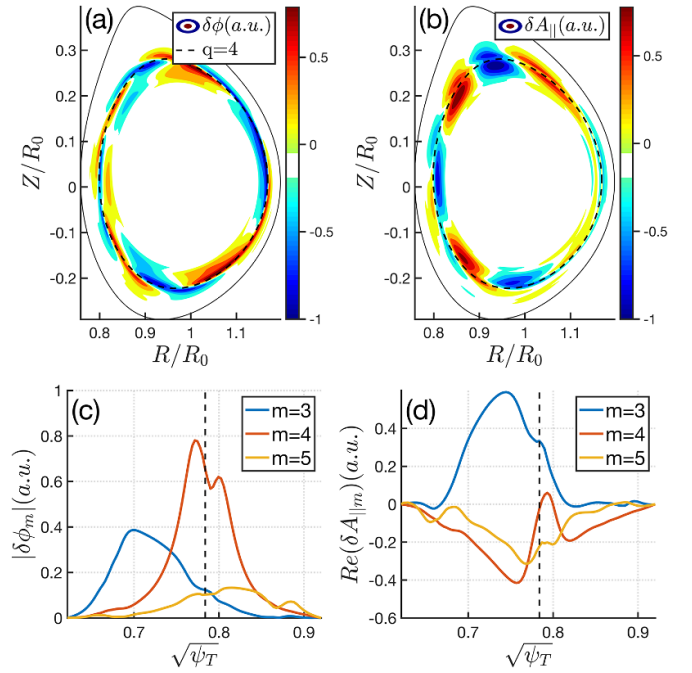


**Figure 17.**  $m/n = 4/1$  e-BAE mode structure with EE drive at the red pentagram location of minimal  $\beta_{h,crit}$  in figure 15(b).

The MAS simulations are performed with  $\lambda_{low} = 1$ , and the parametric dependencies of e-BAE  $\omega_r$  and  $\gamma$  on  $n_{h0}$  and  $T_{h0}$  are shown in figure 15. It is seen that as  $\beta_h = 8\pi n_{h0} T_{h0} / B_0^2$  increases,  $\omega_r$  slightly decreases from the continuum accumulation point (CAP) near 32 kHz, while  $\gamma/\omega_r$  quickly increases from negative damping to positive growth, where the cyan solid line indicates the marginal stable regime in figure 15(b). The  $T_{h0}/T_{e0,a}$  range for e-BAE excitation is [15, 35] along the cyan solid line that corresponds to [63 keV, 149 keV], which partially overlaps with experimental measurements in figure 3 of [10], and there exists a minimal value of  $\beta_{h,crit} \approx 0.76 \beta_{e0,a}$  (where  $\beta_{e0,a}$  is on-axis thermal electron pressure ratio) for e-BAE excitation indicated by the red pentagram in figure 15(b). Given the fact that precession frequency is proportional to

both  $n$  number and energy, both upper and lower limits of EE temperature range for  $n = 2$  e-BAE excitation decrease by a half than that of  $n = 1$  case, which agrees with the experimental measurements of  $T_{h0} < 63$  keV part. The  $m/n = 4/1$  BAE mode structure in the absence of EE drive is shown in figure 16, and the  $m/n = 4/1$  e-BAE mode structure with EE drive at minimal  $\beta_{h,crit}$  location in figure 15(b) is shown in figure 17. The e-BAE exhibits larger amplitudes of  $m = 3$  and  $m = 5$  sideband harmonics and radially broader mode structure, compared to BAE in the absence of EE drive. Note that e-BAE in figure 17 is more radially localized compared to e-BAE in figure 6, because the magnetic shear in EAST is large and the neighboring rational surfaces are more close to each other.

## 5. Summary

In this work, we have formulated a novel fluid-kinetic hybrid model that couples drift-kinetic EEs to the Landau-fluid bulk plasmas for simulating kinetic-MHD processes in a non-perturbative manner, which retains the total EE adiabatic response and deeply-trapped EE non-adiabatic response with precessional drift resonance. The new model has been implemented and verified in the eigenvalue code MAS [25] with practical applications that cover MHD modes, AEs and drift wave instabilities, and the main characteristics are summarized as follows.

- 1. Drift-kinetic description of EE responses.** The EE perturbed distribution is solved from the drift-kinetic equation with well-circulating approximation for passing EEs and deeply-trapped approximation for trapped EEs, which keeps the EE kinetic effect of precession drift resonance that is responsible for the excitations of most EE-driven AEs, and the EE fluid effects such as adiabatic and convective responses. Although the well-circulating and deeply-trapped approximations are made in the derivation, it is shown that the EE moments integrated from the perturbed distribution, i.e. perturbed density, parallel current and pressure, can well guarantee the conservation property of EE continuity equation.
- 2. Improved deeply-trapped model.** The deeply-trapped approximation is applied for deriving the EE drive terms with dominant precessional drift resonance, which has computational advantage because the heavily numerical integration along the realistic particle orbit is not involved. Specifically, this approximation is made for both the calculation of precession frequency (i.e.  $\bar{\omega}_d$ ) and bounce average operations on electromagnetic fields (i.e.  $\bar{\delta\phi}$ ,  $\bar{\delta\psi}$  and  $\bar{\omega}_d\delta\psi$ ), where we induce a control parameter  $\lambda_{\text{low}}$  to calculate the 2D poloidal profile of deeply-trapped particle fraction  $f_t$ , namely, only keep the trapped particles that satisfy  $\bar{\omega}_d/\omega_{d0} \sim 1$  and  $|\theta| \ll 1/|nq - m|$  simultaneously. By improving the accuracy of deeply-trapped approximation with above two constraints, MAS simulations of e-BAE mode structure and dispersion relation show good agreements with GTC gyrokinetic PIC simulations.
- 3. Non-perturbative approach.** The EEs are self-consistently incorporated in MAS computations of mode structure, real frequency and growth rate. The non-perturbative effects of EEs on e-BAE mode structures and corresponding radial variations of phase angle profiles are demonstrated. In particular, the EE-KPC term is found to effectively twist the e-BAE global mode structure and break the poloidal up-down symmetry due to the anti-Hermitian contributions to the dielectric tensor, while EE-IC term represents the fluid convective response and thus compensate the Hermitian part, which leads to the mode structure to be more symmetric. The EE-KPC term is also responsible for the large radial variations of phase angle, of which poloidal phase shifts at different radial locations are consistent with the ‘boomerang’ shape mode structure.

- 4. Comprehensive damping and drive effects.** The original Landau-fluid model for bulk plasmas in MAS [25] has already incorporated the important continuum damping, Landau damping and radiative damping. The newly formulated fluid-kinetic hybrid model combines the EE drive together with various damping mechanisms, which is more reliable for explaining the marginal stable AEs observed in experiments and is useful for evaluating the EE density and temperature thresholds for AE excitation. For comparison, the bulk plasma damping physics are commonly absent in traditional kinetic-MHD hybrid simulations that might affect the unstable spectra.

Thanks to the high efficiency of eigenvalue approach in computation, the upgraded MAS model is suitable for fast parameter scans of deeply-trapped EE relevant problems that attract attentions in recent experiments. Meanwhile, the coupling scheme of EE and bulk plasma can be used for other EE distributions and/or full EE dynamics in phase space, e.g. showing-down distribution and barely circulating/trapped EEs [48].

## Acknowledgments

This work is supported by the National MCF Energy R&D Program under Grant No. 2018YFE0304100; National Natural Science Foundation of China under Grant Nos. 12275351, 11905290 and 11835016; and the start-up funding of Institute of Physics, Chinese Academy of Sciences under Grant No. Y9K5011R21. We would like to thank useful discussions with Zhixin Lu, Huishan Cai, Yong Xiao and Ruirui Ma.

## Appendix A. Typical EP orbits and resonances with AEs in fusion devices

It is useful to compare the wave-particle interactions of typical EP species and AEs in present-day tokamaks and future fusion reactor. Besides EE produced from ECRH and LHCD as mentioned in introduction, the dominant EP species also include EIs from neutral beam injection (NBI) and ion cyclotron resonance heating (ICRH), and the energetic fusion products, i.e. alpha particles. We calculate orbits of different EP species, Alfvén continua, and wave-particle resonances based on experimental geometries that are linked to specific EP physics, namely, DIII-D shot #159243 at  $t = 805$  ms for NBI ions [49], EAST shot #85289 at  $t = 4090$  ms for EEs [10], and ITER 15 MA baseline scenario for alpha particles [50]. In the phase space of  $(P_\zeta, \lambda, E)$ , each EP particle is loaded at the same values of  $P_\zeta/\psi_w = -0.5$  and  $\lambda = 1$ , where  $P_\zeta = g\rho_{||} - \psi$  is the canonical angular momentum,  $\psi_w$  is the poloidal magnetic flux at the wall location that differs with specific devices, and  $\lambda = \mu B_a/E$  is the pitch angle (Note that energy  $E = 0.5$  mv<sup>2</sup> is defined with mass in appendix A). The energies of NBI ion, EE and alpha particle are  $E_{\text{NBI}} = 60$  keV,  $E_{\text{EE}} = 100$  keV and  $E_\alpha = 3.5$  MeV, respectively, of which orbits are shown in figures 18(a1)–(a3). It is clearly seen that alpha particle

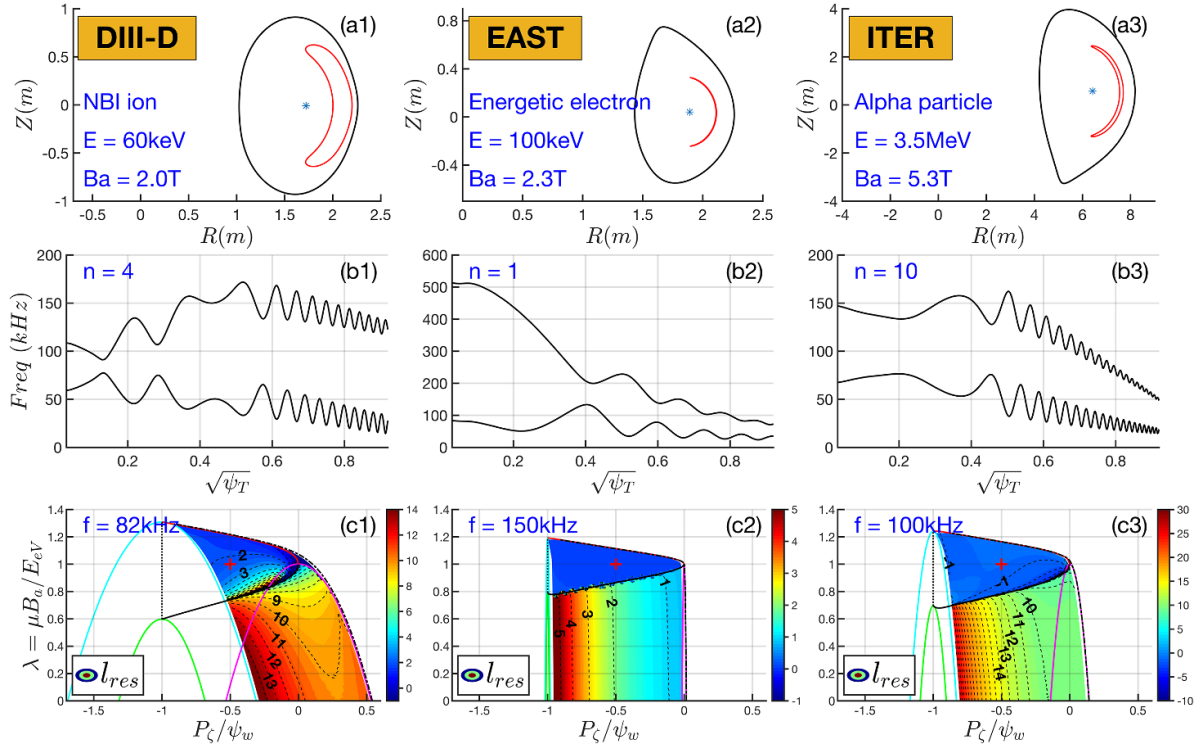


**Figure 18.** The typical EP orbits with  $P_c/\psi_w = -0.5$  and  $\lambda = \mu B_a/E = 1$  in fusion devices: (a1) NBI ion in DIII-D ( $E = 60$  keV), (a2) EE in EAST ( $E = 100$  keV) and (a3) alpha particle in ITER ( $E = 3.5$  MeV). The Alfvén continua calculated using experimental equilibria of (b1) DIII-D, (b2) EAST and (b3) ITER. The resonance condition represented by  $l_{\text{res}}$  harmonics on  $(P_c, \lambda)$  plane at fixed  $E$ : (c1)  $n = 4$ ,  $f = 82$  kHz RSAE resonates with NBI ion in DIII-D, (c2)  $n = 1$ ,  $f = 150$  kHz TAE resonates with EE in EAST, and (c3)  $n = 10$ ,  $f = 100$  kHz TAE resonates with alpha particle in ITER. The red plus signs indicate phase space locations of the example EP orbits, and the solid cyan, green, magenta, black lines correspond to right wall, left wall, magnetic axis and trapped-passing boundaries.

in ITER has small dimensionless orbit that is similar to EE in EAST, which indicates that both alpha particle and EE interact with waves locally in the radial direction of tokamak, in contrast the orbit width of 60 keV NBI ion in DIII-D is on the same order of minor radius, resulting in additional physics associated to nonlocal effects [13]. The TAE gaps of Alfvén continua are investigated based on ideal MHD model with slow sound approximation in figures 18(b1)–(b3), and the  $n$  numbers are chosen with considering unstable AEs spectra excited by corresponding EP species. The results show TAE-gap center frequency  $f_{\text{TAE}} = V_A/(4\pi qR)$  in ITER is close to present-day tokamaks since Alfvén velocity  $V_A$  relies on both magnetic field strength and density. The generalized wave–particle resonance condition can be written as [51]

$$\omega = n\omega_\zeta + l_{\text{res}}\omega_\theta, \quad (70)$$

where  $\omega_\zeta = \Delta\zeta/\tau_b$  and  $\omega_\theta = 2\pi/\tau_b$  are the toroidal and poloidal transit frequencies,  $\tau_b = \oint(\frac{dl}{v_{||}})$  is the poloidal transit time,  $\omega$  and  $n$  are the wave frequency and toroidal mode number. The occurrence of wave–particle resonance requires equation (70) is satisfied with integer  $l_{\text{res}}$ , i.e. the wave frequency matches with EP particle orbital frequencies. To identify the representative wave–particle resonances in each device, we choose  $n = 4$  and  $f = 82$  kHz RSAE for  $E = 60$

keV NBI-ion in DIII-D [52],  $n = 1$  and  $f = 150$  kHz TAE for  $E = 100$  keV EE in EAST, and  $n = 10$  and  $f = 100$  kHz TAE for  $E = 3.5$  MeV alpha particle in ITER, respectively, where the resonance lines and topological boundaries of phase space are shown in figures 18(c1)–(c3). There are large confined domains for both EEs in EAST and alpha particles in ITER, and equation (70) reduces to  $\omega = n\omega_\zeta$  (i.e.  $l_{\text{res}} = 0$ ) for most trapped-confined orbits that drive AEs and  $n\omega_\zeta + l_{\text{res}}\omega_\theta = 0$  (i.e.  $\omega \ll |n\omega_\zeta|$  and  $\omega \ll |l_{\text{res}}\omega_\theta|$ ) for passing-confined orbits known as momentum-altering resonance [4], which differs from NBI-ions in DIII-D with noteworthy loss region and resonance lines described by origin equation (70) with  $l_{\text{res}} \neq 0$ . So far, we have numerically show that EE-AE resonance in present-day tokamak can be analogous to alpha-AE resonance in future fusion reactor based on the realistic experimental parameters.

## Appendix B. Comparison of i-BAE and e-BAE properties using GTC simulations

To delineate the differences between EI-driven BAE (i-BAE) and e-BAE, we perform GTC simulations of i-BAEs using the same parameters in section 4.2. It is found that i-BAEs also exhibit ‘boomerang’ (triangularity) shape poloidal mode structures as shown in figures 19(a1)–(d1), however, the tip

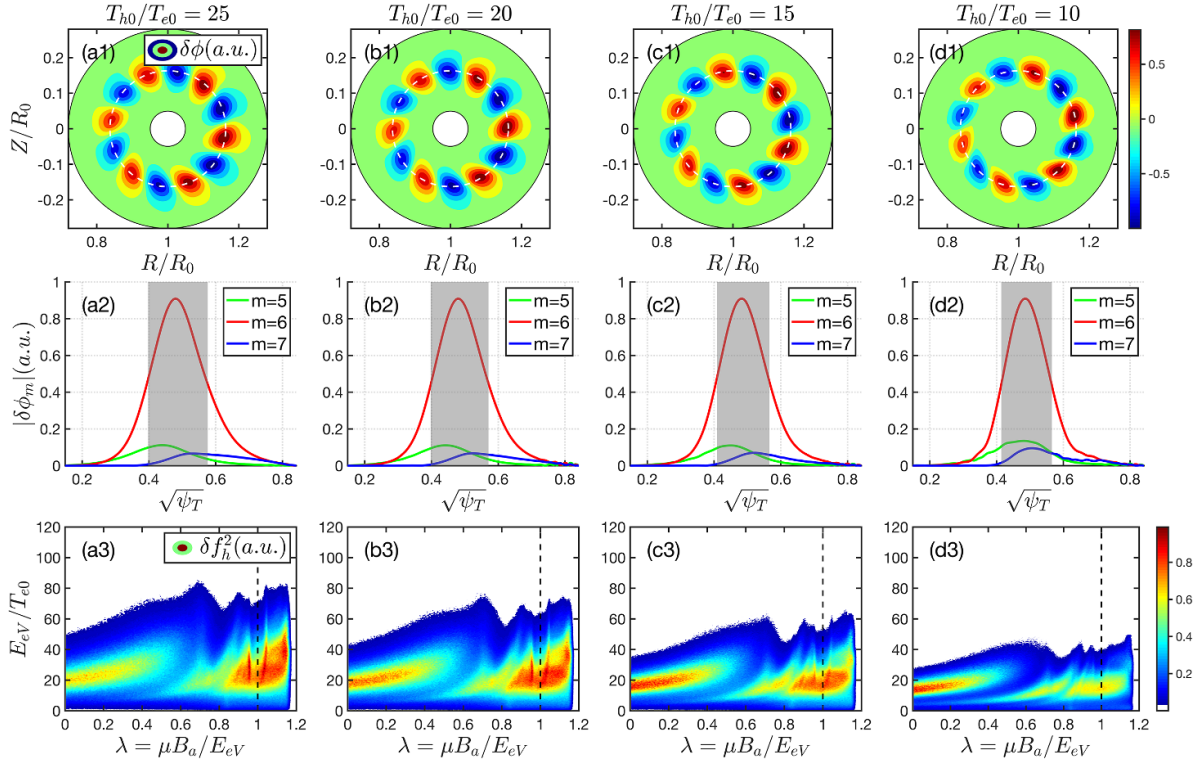


**Figure 19.** GTC simulation of  $n = 3$  i-BAE with different EI temperatures, and  $T_{h0}/T_{e0} = 25$ ,  $T_{h0}/T_{e0} = 20$ ,  $T_{h0}/T_{e0} = 15$  and  $T_{h0}/T_{e0} = 10$  are used from the left to the right column. The captions of first and second rows are the same as figure 7, and the bottom row represents  $\delta f_h^2$  structure in  $(E, \lambda)$  phase space for EIs.

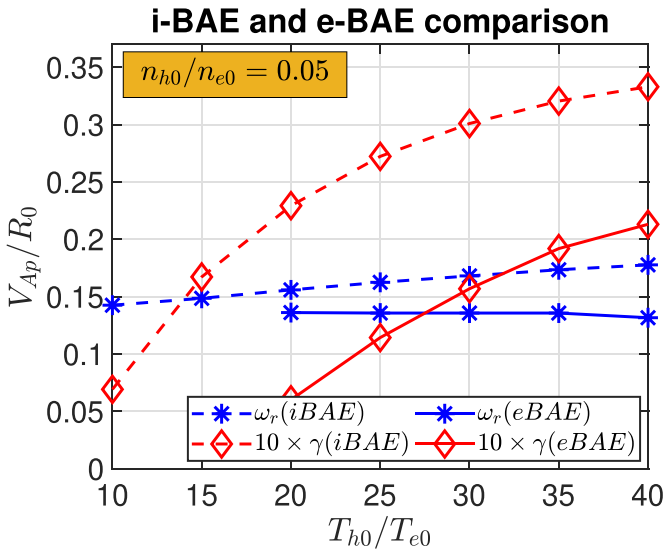


**Figure 20.** Comparison of i-BAE and e-BAE dispersion relations from GTC simulations.

direction is opposite to e-BAE in figure 7(d1). In contrast to the unique precessional drift resonance for e-BAE excitation by EEs, both passing and trapped EIs can resonate with BAEs as shown in figures 19(a3)–(d3), since the ion mass is much larger than electron, the transit and bounce frequencies of EIs can be close to BAE frequency. As EI temperature decreases, the ‘boomerang’ shape of i-BAE poloidal mode

structure becomes more clear, together with a narrower radial width, and the dominant wave–particle interaction moves from bounce–precession resonance to transit resonance. Moreover, the dispersion curves of i-BAE and e-BAE are compared in figure 20, it is seen that  $\omega_r$  of i-BAE can increase slowly with EP temperature while  $\omega_r$  of e-BAE almost remains unchanged, and  $\gamma$  of i-BAE is much larger than e-BAE due to the larger free energy released through multiple resonance channels.

#### ORCID iDs

W.L. Zhang <https://orcid.org/0000-0002-7136-2119>  
 Z.Y. Qiu <https://orcid.org/0000-0002-7548-8819>  
 W. Chen <https://orcid.org/0000-0002-9382-6295>  
 X. Zhu <https://orcid.org/0000-0002-8577-5803>

#### References

- [1] Chen L. and Zonca F. 2016 Physics of Alfvén waves and energetic particles in burning plasmas *Rev. Mod. Phys.* **88** 015008
- [2] Fasoli A. et al 2007 Progress in the ITER physics basis—Chapter 5 Physics of energetic ions *Nucl. Fusion* **47** S264
- [3] Heidbrink W.W. 2008 Basic physics of Alfvén instabilities driven by energetic particles in toroidally confined plasmas *Phys. Plasmas* **15** 055501
- [4] Heidbrink W.W. and White R.B. 2020 Mechanisms of energetic-particle transport in magnetically confined plasmas *Phys. Plasmas* **27** 030901

- [5] Chen W. *et al* 2010 Beta-induced Alfvén eigenmodes destabilized by energetic electrons in a tokamak plasma *Phys. Rev. Lett.* **105** 185004
- [6] Chen W. *et al* 2011 Destabilization of beta-induced Alfvén eigenmodes in the HL-2A tokamak *Nucl. Fusion* **51** 063010
- [7] Yu L.M. *et al* 2018 Toroidal Alfvén eigenmode driven by energetic electrons during high-power auxiliary heating on HL-2A *Phys. Plasmas* **25** 012112
- [8] Hu W. *et al* 2018 Observation of Alfvén eigenmodes driven by fast electrons during lower hybrid wave heating in EAST plasmas *Nucl. Fusion* **58** 096032
- [9] Chu N. *et al* 2018 Observation of toroidal Alfvén eigenmode excited by energetic electrons induced by static magnetic perturbations in the EAST tokamak *Nucl. Fusion* **58** 104004
- [10] Zhao N. *et al* 2021 Multiple Alfvén eigenmodes induced by energetic electrons and nonlinear mode couplings in EAST radio-frequency heated H-mode plasmas *Nucl. Fusion* **61** 046013
- [11] Chu N. *et al* 2021 Observation of TAE mode driven by off-axis ECRH induced barely trapped energetic electrons in EAST tokamak *Nucl. Fusion* **61** 046021
- [12] Zhu X. *et al* 2022 Nonlinear mode couplings between geodesic acoustic mode and toroidal Alfvén eigenmodes in the EAST tokamak *Phys. Plasmas* **29** 062504
- [13] Zonca F. *et al* 2007 Electron fishbones: theory and experimental evidence *Nucl. Fusion* **47** 1588
- [14] Ma R., Qiu Z., Li Y. and Chen W. 2020 Destabilization of beta-induced Alfvén eigenmodes by energetic trapped electrons in tokamak *Nucl. Fusion* **60** 056019
- [15] Ma R., Qiu Z., Li Y. and Chen W. 2021 Global theory of beta-induced Alfvén eigenmode excited by trapped energetic electrons *Nucl. Fusion* **61** 036014
- [16] Qiu Z., Chen L., Zonca F. and Ma R. 2020 Zero frequency zonal flow excitation by energetic electron driven beta-induced Alfvén eigenmode *Plasma Phys. Control. Fusion* **62** 105012
- [17] Cheng J.Y., Zhang W.L., Lin Z., Holod I., Li D., Chen Y. and Cao J. 2016 Gyrokinetic particle simulation of fast-electron driven beta-induced Alfvén eigenmode *Phys. Plasmas* **23** 052504
- [18] Cheng J.Y., Zhang W.L., Lin Z., Li D., Dong C. and Cao J. 2017 Nonlinear co-existence of beta-induced Alfvén eigenmodes and beta-induced Alfvén-acoustic eigenmodes *Phys. Plasmas* **24** 092516
- [19] Wang J.L., Todo Y., Wang H. and Wang Z.-X. 2020 Simulation of Alfvén eigenmodes destabilized by energetic electrons in tokamak plasmas *Nucl. Fusion* **60** 112012
- [20] Wang J.L., Todo Y., Wang H., Wang Z.-X. and Iduoukass M. 2020 Stabilization of energetic-ion driven toroidal Alfvén eigenmode by energetic electrons in tokamak plasmas *Nucl. Fusion* **60** 106004
- [21] Lee W.W., Lewandowski J.L.V., Hahn T.S. and Lin Z. 2001 Shear-Alfvén waves in gyrokinetic plasmas *Phys. Plasmas* **8** 4435
- [22] Lauber P., Günter S., Könies A. and Pinches S.D. 2007 LIGKA: a linear gyrokinetic code for the description of background kinetic and fast particle effects on the MHD stability in tokamaks *J. Comput. Phys.* **226** 447
- [23] Cheng C.Z. 1992 Kinetic extensions of magnetohydrodynamics for axisymmetric toroidal plasmas *Phys. Rep.* **211** 1
- [24] Borba D. and Kerner W. 1999 CASTOR-K: stability analysis of Alfvén eigenmodes in the presence of energetic ions in tokamaks *J. Comput. Phys.* **153** 101
- [25] Bao J. *et al* 2023 MAS: a versatile Landau-fluid eigenvalue code for plasma stability analysis in general geometry *Nucl. Fusion* **63** 076021
- [26] Brochard G. *et al* 2022 Verification and validation of linear gyrokinetic and kinetic-MHD simulations for internal kinetic instability in DIII-D tokamak *Nucl. Fusion* **62** 036021
- [27] Chen L. and Hasegawa A. 1991 Kinetic theory of geomagnetic pulsations: 1. Internal excitations by energetic particles *J. Geophys. Res. Space Phys.* **96** 1503
- [28] Zonca F., Chen L. and Santoro R.A. 1996 Kinetic theory of low-frequency Alfvén modes in tokamaks *Plasma Phys. Control. Fusion* **38** 2011
- [29] Bao J., Liu D. and Lin Z. 2017 A conservative scheme of drift kinetic electrons for gyrokinetic simulation of kinetic-MHD processes in toroidal plasmas *Phys. Plasmas* **24** 102516
- [30] Tsai S. and Chen L. 1993 Theory of kinetic ballooning modes excited by energy particles in tokamaks *Phys. Fluids B* **5** 3284
- [31] Chavdarovski I. and Zonca F. 2009 Effects of trapped particle dynamics on the structures of a low-frequency shear Alfvén continuous spectrum *Plasma Phys. Control. Fusion* **51** 115001
- [32] Hammett G.W. and Perkins F.W. 1990 Fluid moment models for Landau damping with application to the ion-temperature-gradient instability *Phys. Rev. Lett.* **64** 3019
- [33] White R.B. 2013 *Theory Of Toroidally Confined Plasmas* (World Scientific Publishing Company)
- [34] Taimourzadeh S. *et al* 2019 Verification and validation of integrated simulation of energetic particles in fusion plasmas *Nucl. Fusion* **59** 066006
- [35] Deng W., Lin Z. and Holod I. 2012 Gyrokinetic simulation model for kinetic magnetohydrodynamic processes in magnetized plasmas *Nucl. Fusion* **52** 023005
- [36] Dong G., Wei X.S., Bao J., Brochard G., Lin Z. and Tang W.M. 2021 Deep learning based surrogate models for first-principles global simulations of fusion plasmas *Nucl. Fusion* **61** 126061
- [37] Berk H.L., Van Dam J.W., Guo Z. and Lindberg D.M. 1991 Continuum damping of low-n toroidicity-induced shear Alfvén eigenmodes *Phys. Fluids B* **4** 1806
- [38] Rosenbluth M.N., Berk H.L., Van Dam J.W. and Lindberg D.M. 1992 Mode structure and continuum damping of high-n toroidal Alfvén eigenmodes *Phys. Fluids B* **4** 2189
- [39] Mett R.R. and Mahajan S.M. 1992 Kinetic theory of toroidicity-induced Alfvén eigenmodes *Phys. Fluids B* **4** 2885
- [40] Fu G.Y., Berk H.L. and Pletzer A. 2005 Kinetic damping of toroidal Alfvén eigenmodes *Phys. Plasmas* **12** 082505
- [41] Lauber P., Günter S. and Pinches S.D. 2005 Kinetic properties of shear Alfvén eigenmodes in tokamak plasmas *Phys. Plasmas* **12** 122501
- [42] Ma R., Zonca F. and Chen L. 2015 Global theory of beta-induced Alfvén eigenmode excited by energetic ions *Phys. Plasmas* **22** 092501
- [43] Wang Z., Lin Z., Holod I., Heidbrink W.W., Tobias B., Van Zeeland M. and Austin M.E. 2013 Radial localization of toroidicity-induced Alfvén eigenmodes *Phys. Rev. Lett.* **111** 145003
- [44] Lu Z.X., Wang X., Lauber P. and Zonca F. 2018 Kinetic effects of thermal ions and energetic particles on discrete kinetic BAE mode generation and symmetry breaking *Nucl. Fusion* **58** 082021
- [45] Tobias B., Classen I., Domier C., Heidbrink W.W., Luhmann Jr N., Nazikian R., Park H., Spong D.A. and Van Zeeland M. 2011 Fast ion induced shearing of 2D Alfvén eigenmodes measured by electron cyclotron emission imaging *Phys. Rev. Lett.* **106** 075003
- [46] Heidbrink W.W., Hansen E.C., Austin M.E., Kramer G.J. and Van Zeeland M.A. 2022 The radial phase variation of

- reversed-shear and toroidicity-induced Alfvén eigenmodes in DIII-D *Nucl. Fusion* **62** 066020
- [47] Berk H.L., Breizman B.N. and Pekker M. 1996 Nonlinear dynamics of a driven mode near marginal stability *Phys. Rev. Lett.* **76** 1256
- [48] Wang T., Zhu X., Zeng L., Briguglio S., Vlad G., Zonca F. and Qiu Z. 2023 Excitation of toroidal Alfvén eigenmode by barely circulating energetic electrons in low density plasmas *Plasma Phys. Control. Fusion* **65** 055026
- [49] Collins C. *et al* 2016 Observation of critical-gradient behavior in Alfvén-eigenmode-induced fast-ion transport *Phys. Rev. Lett.* **116** 095001
- [50] Polevoi A.R., Medvedev S.Y., Mukhovatov V.S., Kukushkin A.S., Murakami Y., Shimada M. and Ivanov A.A. 2002 ITER confinement and stability modelling *J. Fusion Res.* **5** 82–97
- [51] Porcelli F., Stankiewicz R., Kerner W. and Berk H.L. 1994 Solution of the drift-kinetic equation for global plasma modes and finite particle orbit widths *Phys. Plasmas* **1** 470
- [52] Meng G., Gorelenkov N.N., Duarte V.N., Berk H.L., White R.B. and Wang X.G. 2018 Resonance frequency broadening of wave-particle interaction in tokamaks due to Alfvénic eigenmode *Nucl. Fusion* **58** 082017